Spectrum Sensing for Cognitive Radio

The utility of the multitaper method and cyclostationarity for sensing the radio spectrum, including the digital TV spectrum, is studied theoretically and experimentally.

By Simon Haykin, *Life Fellow IEEE*, David J. Thomson, *Fellow IEEE*, and Jeffrey H. Reed, *Fellow IEEE*

ABSTRACT | Spectrum sensing is the very task upon which the entire operation of cognitive radio rests. For cognitive radio to fulfill the potential it offers to solve the spectrum underutilization problem and do so in a reliable and computationally feasible manner, we require a spectrum sensor that detects spectrum holes (i.e., underutilized subbands of the radio spectrum), provides high spectral-resolution capability, estimates the average power in each subband of the spectrum, and identifies the unknown directions of interfering signals. Cyclostationarity is another desirable property that could be used for signal detection and classification. The multitaper method (MTM) for nonparametric spectral estimation accomplishes these tasks accurately, effectively, robustly, and in a computationally feasible manner. The objectives of this paper are to present: 1) tutorial exposition of the MTM, which is expandable to perform space–time processing and time–frequency analysis; 2) cyclostationarity, viewed from the Loève and Fourier perspectives; and 3) experimental results, using Advanced Television Systems Committee digital television and generic land mobile radio signals, followed by a discussion of the effects of Rayleigh fading.

S. Haykin is with the Cognitive Systems Laboratory, McMaster University, Hamilton, ON L8S 4K1, Canada (e-mail: haykin@mcmaster.ca).
D. J. Thomson is with Queen's University, Kingston, ON, Canada.
J. H. Reed is with the Bradley Department of Electrical and Computer Engineering, Virginia Polytechnic and State University, Blacksburg, VA 24061 USA.

I. INTRODUCTION

The usable electromagnetic radio spectrum—a precious natural resource—is of limited physical extent. However, wireless devices and applications are increasing daily. It is therefore not surprising that we are facing a difficult situation in wireless communications. Moreover, given the reality that, currently, the licensed part of the radio spectrum is poorly utilized [1], this situation will only get worse unless we find new practical means for improved utilization of the spectrum. *Cognitive radio,* a new and novel way of thinking about wireless communications, has the potential to become the solution to the *spectrum underutilization problem* [2], [3].

Building on spectrum sensing and other basic tasks, the ultimate objective of a cognitive radio network is twofold:

- provide *highly reliable communication* for all users of the network, wherever and whenever needed;
- facilitate *efficient utilization of the radio spectrum* in a fair-minded and cost-effective manner.

A. Spectrum Sensing

In this paper, we focus attention on the particular task on which the very essence of cognitive radio rests: *spectrum sensing,* defined as the task of finding *spectrum holes* by sensing the radio spectrum in the local neighborhood of the cognitive radio receiver in an unsupervised manner. The term "spectrum holes" stands for those subbands of the radio spectrum that are underutilized (in part

or in full) at a particular instant of time and specific geographic location. To be specific, the task of spectrum sensing involves the following subtasks:

1) detection of spectrum holes;
2) spectral resolution of each spectrum hole;
3) estimation of the spatial directions of incoming interferes;
4) signal classification.

The subtask of spectrum-hole detection is, at its simplest form, when the focus is on a white space (i.e., a subband that is only occupied by white noise). Specifically, the detection of a white space may be performed by using a radiometer, which is well known for its energy-detection capability [4], [5]. Alternatively, we may resort to the use of *cyclostationarity,* which is an inherent property of *digital modulated signals* that naturally occur in the transmission of communication signals over a wireless channel [6], [7]. In both of these two approaches to spectrum sensing, the detection of a spectrum hole boils down to a *binary hypothesis-testing problem*. Specifically, hypothesis H_1 refers to the presence of a primary user's signal (i.e., the subband under test is occupied) and hypothesis H_0 refers to the presence of ambient noise (i.e., the subband is a white space). The cyclostationarity approach to detection has an advantage over the energy-detection approach in that it is also capable of signal classification and has the ability to distinguish cochannel interference.

The use of both of these approaches is confined to white spaces only, which limits the scope of their spectrum-sensing capabilities. In order to further refine the detection of white spaces and broaden the scope of spectrum sensing so as to also include the possible employment of gray spaces (i.e., subbands of the spectrum that contain noise as well as interfering signals), we may have to resort to a sensing technique that includes spectrum estimation.

Spectrum estimation can be of a *parametric* kind, which requires modeling the stochastic process of interest; a widely used example is *autoregressive* (AR) modeling. Alternatively, spectrum estimation can be of a *nonparametric* kind, bypassing the need for modeling, and therefore working directly on the stochastic process under study. Given the notoriously unreliable nature of wireless channels, compounded by the uncertainty of accessing underutilized subbands of the radio spectrum by cognitive radios that come and go, the nonparametric approach to spectrum estimation is a preferred choice for spectrum sensing.

Most importantly, with emphasis on reliable communications and efficient utilization of spectrum holes, we need a nonparametric method for spectrum sensing that is *reliable,* capable of *high spectral resolution* in both average power and frequency, and *computationally feasible in real-time*. A spectral estimator that satisfies these requirements is the *multitaper method* or *multitaper spectral estimator* [8]; hereafter, both terminologies are used interchangeably. Another attribute of the multitaper method (MTM) is that it lends itself naturally to *space–time processing,* whereby the direction for a reliable communication link can be established; in effect, the cognitive radio is provided with a *sense of direction*. Furthermore, by combining the MTM with the *Loève transform,* a cognitive radio is enabled to perform *time–frequency analysis* (TFA) and thereby provide the property of cyclostationarity when a digital modulated signal is present. Putting all these pieces together, in MTM we have the making of an *integrated multifunction signal processor* that is wholly *nonparametric* and therefore *robust*. Most importantly, this integrated receiver accounts for all three essential dimensions of sensing: time, frequency, and space.

In addition to the MTM as a tool for spectrum sensing, this paper also discusses the idea of cyclostationarity viewed in a Fourier-theoretic framework. Cyclostationarity has a large body of literature that extends over 50 years, much of which has focused on Fourier theory [9].

Most importantly, the study of the MTM and cyclostationarity as tools for spectrum sensing is supported with experimental results, using Advanced Television Systems Committee (ATSC) digital television and generic land mobile radio data.

B. Organization of This Paper

Section II outlines desirable attributes of a spectrum sensor for reliable and efficient utilization of spectrum holes, thereby setting the stage for a tutorial exposition of the MTM in Section III. Given a time series, the MTM produces an estimate of the spectrum of incoming radio-frequency (RF) stimuli as a function of frequency; hence the ability to identify the location of spectrum holes within the radio spectrum. In addition to time as an essential dimension of sensing, cognitive radio also needs to know the spatial distribution of spectrum holes; to this end, the issue of space–time processing is discussed in Section IV. Section V describes time–frequency analysis by combining the MTM with the Loève transform. The discussion of time–frequency analysis is continued in Section VI, wherein the cyclostationarity property of digital modulated signals is viewed in a Fourier-theoretic framework.

With all of this background theory at hand, the stage is set for an experimental study of spectrum sensing in Sections VII and VIII, using data collected from two different communication media, each of which is amenable to cognitive radio in its own way:

- wide-band ASTC digital television signals;
- quadriphase-shift keying (QPSK) used in generic mobile radio.

Section IX addresses spectral considerations in Rayleigh channels. This paper concludes with a summary and discussion in Section X.

II. SPECTRUM SENSING: BACKGROUND CONSIDERATIONS

In terms of occupancy, subbands of the radio spectrum may be categorized as follows.

1) *White spaces,* which are free of RF interferers, except for *noise* due to natural and/or artificial sources.[1]
2) *Gray spaces,* which are partially occupied by interferers as well as noise.
3) *Black spaces,* the contents of which are completely full due to the combined presence of communication and (possibly) interfering signals plus noise.

The transition of all terrestrial television broadcasting from analog to digital, using the ATSC standard, is scheduled for 2009 in North America. Moreover, in November 2008, the Federal Communications Commission (FCC) in the United States ruled that access to the ATSC *digital television* (DTV) band be permitted for wireless devices [11]. Thus, for the first time ever, the way has been opened for the creation of "white spaces" for use by low-power cognitive radios. The availability of these white spaces will naturally vary across time and from one geographic location to another. In reality, noise is not likely to be the sole occupant of the ATSC-DTV band when a TV broadcasting station is switched off. Rather, as illustrated in Section VII, interfering signals of widely varying power levels do exist below the DTV pilot. In other words, some of the subbands constituting the ATSC-DTV band may indeed be "gray" and not "white."

Consider next the commercial cellular networks deployed all over the world. In the current licensing regime, only *primary users* have exclusive rights to transmit. However, it is highly likely to find small spatial footprints in large cells where there are no primary users. Currently, opportunistic low-power usage of the cellular spectrum is not allowed in these areas, even though such usage by cognitive radios in a *femto-* or *picocell* with a small base station is not detrimental to the *primary user* [12]. Thus, spectrum holes may also be found in commercial cellular bands; naturally, spread of the spectrum holes varies over time and space. In any event, *interference* arising from conflict relationships between transmitters (base stations) of various radio infrastructure providers that coexist in a region must be taken into account [13]. Consequently, the spectrum holes found in cellular bands may also be gray spaces.

The important point to take from this discussion is that regardless of where the spectrum holes exist, be they in the ATSC-DTV band or in the cellular band, we are confronted with the practical reality that the spectrum holes may be made up of white or gray spaces. For example, a primary user's signal may be too weak to be of use in the local neighborhood, in which case the same channel may be useful for any low-power secondary user. This possibility may therefore complicate applicability of a simple hypothesis-testing procedure that designates each subband as black (blocked space) or white (exploitable) space, using energy detection or cyclostationarity characterization.

In light of these practical realities, we may now identify the desirable attributes of a nonparametric spectrum sensor for cognitive-radio applications:

1) *Detection of spectrum holes* and their *reliable* classification into white and gray spaces; this classification may require an *accurate estimation of the power spectrum,* particularly when the spectrum hole is of a gray-space kind.
2) *Accurate spectral resolution* of spectrum holes, which is needed for efficient utilization of the radio spectrum.
3) *Estimation of the direction-of-arrival* (DOA) of interferers, which provides the cognitive radio a *sense of direction.*
4) *Time–frequency analysis* for highlighting cyclostationarity, which could be used for the reinforcement of spectrum-hole detection as well as *signal classification* when the subband of interest is occupied by a primary user.

From a practical perspective, it would be desirable not only to carry out these four spectrum-sensing tasks reliably, accurately, effectively, and efficiently but also to have them integrated collectively into a *coherent multifunction signal processor.* The multitaper method, discussed in the next section, provides a *completely nonparametric basis* for the design of such a processor. More will be said on the rationale for this processor as the exposition of spectrum sensing proceeds forward.

III. THE MULTITAPER METHOD FOR SPECTRUM SENSING

In the older spectrum-estimation literature on nonparametric methods, it was emphasized that the estimation problem is difficult because of the *bias-variance dilemma,* which encompasses the interplay between two conflicting statistical issues.

- *Bias* of the power-spectrum estimate of a time series due to the sidelobe-leakage phenomenon, the effect of which is reduced by tapering (i.e., *windowing*) the time series.

---

[1]The most common natural source of noise encountered at the front end of communication receivers is *thermal noise,* which is justifiably modeled as *additive white Gaussian noise.*

By far the most important artificial source of noise in mobile communications is *man-made noise,* which is radiated by different kinds of electrical equipment across a frequency band extending from about 2 to about 500 MHz [10]. Unlike thermal noise, man-made noise is impulsive in nature; hence the reference to it as *impulsive noise.* In urban areas, the impulsive noise generated by motor vehicles is a major source of interference to mobile communications.

With the statistics of impulsive noise being radically different from the Gaussian characterization of thermal noise, the modeling of noise in a white space due to the combined presence of Gaussian noise and impulsive noise in urban areas may complicate binary hypothesis-testing procedures for spectrum holes.

- The cost incurred by this improvement is an increase in *variance* of the estimate, which is due to the loss of information resulting from a reduction in the effective sample size. Furthermore, because of the apparent arbitrariness of many of the early tapers, there was opposition to the idea of tapering [14].

How, then, can we resolve this dilemma by mitigating the loss of information due to tapering? The answer to this fundamental question lies in the principled use of *multiple orthonormal tapers (windows),* an idea that is embodied in the multitaper spectral estimation procedure [8]. Specifically, the procedure linearly expands the part of the time series in a fixed bandwidth extending from $f - W$ to $f + W$ (centered on some frequency f) in a special family of sequences known as the *Slepian sequences;* these sequences are also referred to in the literature as *discrete prolate spheroidal wave functions* [15]. The remarkable property of Slepian sequences is that their Fourier transforms have the maximal energy concentration in the bandwidth $2W$ (centered on f) under a finite sample-size constraint. This property, in turn, permits trading spectral resolution for improved spectral characteristics, that is, reduced variance of the spectral estimate without compromising the bias of the estimate. In other words, the old bias–variance tradeoff is now replaced with a bias–resolution tradeoff, which, once properly taken care of, also solves the variance problem. The multitaper method can thereby produce an accurate estimate of the desired power spectrum.

A. Attributes of Multitaper Spectral Estimation

From a practical perspective, multitaper spectral estimators have several desirable features [16].

1) In contrast to the conventional use of the *weighted overlapped segment averaging* (WOSA) procedure due to Welch [17] that can still suffer from leakage, the multitaper spectral estimator is applicable in an "automatic" fashion.

2) In multitaper spectral estimation, the bias is decomposed into two quantifiable components:
    - *local bias* due to frequency components residing inside the user-selectable band from $f - W$ to $f + W$;
    - *broadband bias* due to frequency components found outside this band.

3) The *resolution* of multitaper spectral estimators is naturally defined by the bandwidth of the passband, namely, $2W$.

4) Multitaper spectral estimators offer an easy-to-quantify *tradeoff between bias and variance.*

5) Direct spectrum estimation can be performed with more than just two *degrees of freedom;* typically, the degrees of freedom vary from six to ten, depending on the time–bandwidth product used in the estimation.

6) An internal estimate of the variance of the multitaper spectral estimate can be computed by using the so-called *jackknifing technique* [18].

7) Multitaper spectral estimation may be viewed as a form of *regularization;* in other words, multitaper spectral estimation provides an analytic basis for computing the best approximation to a desired power spectrum, which is not possible from single-taper estimates [16].

8) Multitaper spectral estimates can be used to distinguish line components within the band $[f - W, f + W]$ by including the harmonic *F*-test, as demonstrated in Section VII.

With these highly desirable features built into the composition of a multitaper spectral estimator, it is therefore not surprising to find that it outperforms other well-known spectral estimators, as discussed later in the section.

B. Multitaper Spectral Estimation Theory

Let t denote *discrete time*. Let the time series $\{x(t)\}_{t=0}^{N-1}$ represent the *baseband* version of the received RF signal with respect to the center frequency of the RF band under scrutiny; the term "baseband" means that the center frequency of the signal is moved (demodulated) down to 0 Hz. Given this time series, the MTM determines the following parameters [8]:

- an orthonormal sequence of Slepian tapers, denoted by $\{v_t^{(k)}\}_{t=0}^{N-1}$;
- a corresponding set of Fourier transforms

$$X_k(f) = \sum_{t=0}^{N-1} x(t) v_t^{(k)} \exp(-j2\pi ft) \qquad (1)$$

where $k = 0, 1, \ldots, K - 1$. The energy distributions of the *eigenspectra,* defined by $|X_k(f)|^2$ for varying k, are concentrated inside a resolution bandwidth $2W$. The time–bandwidth product

$$C_o = NW$$

bounds the number of tapers (windows) as shown by

$$K \le \lfloor 2NW \rfloor \qquad (2)$$

which, in turn, defines the degrees of freedom (DoF) available for controlling the variance of the multitaper spectral estimator. The choice of parameters C_o and K provides a tradeoff among spectral resolution, bias, and variance. The bias of these estimates is largely controlled

Table 1 Leakage Properties of the Lowest Order Slepian Sequence as a Function of the Time–Bandwidth Product C_o (Column 1). Column 2 Gives the Asymptotic Value of $1 - \lambda_0(C_o)$. and Column 3 is the Same (Total Sidelobe Energy) Expressed in Decibels (Relative to Total Energy in the Signal)

$C_o = NW$	$1 - \lambda_0$	dB
4	3.05×10^{-10}	-95
6	1.31×10^{-15}	-149
8	5.26×10^{-21}	-203
10	2.05×10^{-26}	-257

by the largest eigenvalue, denoted by $\lambda_0(N, W)$, which is given asymptotically by [8]

$$1 - \lambda_0 \approx 4\pi\sqrt{C_o} \exp(-2\pi C_o).$$

This formula gives the fraction of the *total sidelobe energy*, that is, the total leakage into frequencies outside the interval $(-W, W)$; the total sidelobe energy decreases very rapidly with C_o, as can be seen in Table 1. A natural spectral estimate, based on the first few eigenspectra that exhibit the least sidelobe leakage, is given by [8], [16], [19]

$$\hat{S}(f) = \frac{\sum_{k=0}^{K-1} \lambda_k |X_k(f)|^2}{\sum_{k=0}^{K-1} \lambda_k} \quad (3)$$

where $X_k(f)$ is the Fourier transform defined in (1) and λ_k is the eigenvalue associated with the kth eigenspectrum. The denominator in (3) makes the estimator $\hat{S}(f)$ unbiased.

The multitaper spectral estimator of (3) is intuitively appealing in the way it works. As the number of tapers K increases, the eigenvalues decrease, causing the eigenspectra to be more contaminated by leakage. However, the eigenvalues themselves counteract this effect by reducing the weighting applied to higher leakage eigenspectra.

C. Adaptive Modification of Multitaper Spectral Estimation

While the lower order eigenspectra have excellent bias properties, there is some degradation as the order K increases toward the limiting value defined in (2). In [8], a set of *adaptive weights*, denoted by $\{d_k(f)\}$, is introduced to downweight the higher order eigenspectra. Using a mean-square error optimization procedure, the following formula for the weights is derived:

$$d_k(f) = \frac{\sqrt{\lambda_k} S(f)}{\lambda_k S(f) + \mathbf{E}[B_k(f)]}, \quad k = 0, 1, \ldots, K-1 \quad (4)$$

where $S(f)$ is the true power spectrum, $B_k(f)$ is the broadband bias of the kth eigenspectrum, and $\mathbf{E}$ is the

statistical expectation operator. Moreover, we find that

$$\mathbf{E}[B_k(f)] \leq (1 - \lambda_k)\sigma^2, \quad k = 0, 1, \ldots, K-1 \quad (5)$$

where σ^2 is the *process variance*, defined in terms of the time series $x(t)$ by

$$\sigma^2 = \frac{1}{N} \sum_{t=0}^{N-1} |x(t)|^2. \quad (6)$$

In order to compute the adaptive weights $d_k(f)$ using (4), we need to know the true spectrum $S(f)$. Clearly, if we know $S(f)$, then there would be no need to perform any spectrum estimation in the first place. Nevertheless, (4) is useful in setting up an iterative procedure for computing the adaptive spectral estimator, as shown by

$$\hat{S}(f) = \frac{\sum_{k=0}^{K-1} |d_k(f)|^2 \hat{S}_k(f)}{\sum_{k=0}^{K-1} |d_k(f)|^2} \quad (7)$$

where

$$\hat{S}_k(f) = |X_k(f)|^2, \quad k = 0, 1, \ldots, K-1. \quad (8)$$

Note that if we set $|d_k(f)|^2 = \lambda_k$ for all k, then the estimator of (7) reduces to that of (3).

Next, by setting $S(f)$ equal to the spectrum estimate $\hat{S}(f)$ in (4), then substituting the new equation into (7) and collecting terms, we get (after simplifications)

$$\sum_{k=0}^{K-1} \frac{\lambda_k \big(\hat{S}(f) - \hat{S}_k(f)\big)}{\big(\lambda_k \hat{S}(f) + \hat{B}_k(f)\big)^2} = 0 \quad (9)$$

where $\hat{B}_k(f)$ is an estimate of the expectation $\mathbf{E}[B_k(f)]$. Using the upper bound of (5), we may set

$$\hat{B}_k(f) = (1 - \lambda_k)\sigma^2, \quad k = 0, 1, \ldots, K-1. \quad (10)$$

We now have all that we need to solve for the null condition of (9) via the *recursion*

$$\hat{S}^{j+1}(f) = \left[\sum_{k=0}^{K-1} \frac{\lambda_k \hat{S}_k^{(j)}(f)}{\big(\lambda_k \hat{S}^{(j)}(f) + \hat{B}_k(f)\big)^2} \right]$$

$$\times \left[\sum_{k=0}^{K-1} \frac{\lambda_k}{\big(\lambda_k \hat{S}^{(j)}(f) + \hat{B}_k(f)\big)^2} \right]^{-1} \quad (11)$$

where j denotes an iteration step, that is, $j = 0, 1, 2, \ldots$. To initialize the recursion of (11), we may set $\hat{S}^{j}(0)$ equal to the average of the two lowest order eigenspectra. Convergence of the recursion is usually rapid, with successive spectral estimates differing by less than 5% in five to 20 iterations [19], [20]. The result obtained from (11) is substituted into (4) to obtain the desired weights $d_k(f)$.

A useful by-product of the adaptive spectral estimation procedure is a *stability measure of the estimates*, given by

$$\nu(f) = 2 \sum_{k=0}^{K-1} |d_k(f)|^2 \qquad (12)$$

which is the approximate DoF for the estimator $\hat{S}(f)$, expressed as a function of frequency f. If $\overline{\nu}$, denoting the average of $\nu(f)$ over frequency f, is significantly less than $2K$, then the result is an indication that either the bandwidth $2W$ is too small or additional *prewhitening* of the time series $x(t)$ should be used.

The importance of prewhitening cannot be stressed enough for RF data. In essence, prewhitening reduces the dynamic range of the spectrum by filtering the data prior to processing. The resulting residual spectrum is nearly flat or "white." In particular, leakage from strong components is reduced, so that the fine structure of weaker components is more likely to be resolved [19], [20].

D. Summarizing Remarks on the MTM

i) Estimation of the power spectrum based on (3) is said to be *incoherent* because the kth eigenspectrum $|X_k(f)|^2$ ignores phase information for all values of the index k.

ii) For the parameters needed to compute the multitaper spectral estimator (3), recommended values (within each data section) are as follows:
   - parameter $C_o = 4$, possibly extending up to ten;
   - number of Slepian tapers $K = 10$, possibly extending up to 16.

   These values are needed, especially when the dynamic range of the RF data is large.

iii) If, and when, the number of tapers is increased toward the limiting value $2NW$, then the adaptive multitaper spectral estimator should be used.

E. Comparison of the MTM With Other Spectral Estimators

Now that we understand the idea of multitaper spectral estimation, we are ready to compare its performance against other spectral-estimation algorithms. The results described herein summarize previous experimental work that was originally reported in [20] and reproduced in [19].

The test dataset used in the previous work was *Marple's classic synthetic dataset*, the analytic spectrum of which is known exactly [21]. Specifically, the dataset is composed of the following components:
- two complex sinusoids of fractional frequencies 0.2 and 0.21 that are included to test the resolution capability of a spectral estimator;
- two weaker complex sinusoids of 20 dB less power at fractional frequencies −0.15 and 0.1;
- a colored noise process, generated by passing two independently zero-mean real white-noise processes through identical moving-average filters; each filter has an identical raised-cosine frequency response centered at ±0.35 and occupying a bandwidth of 0.3.

Following Marple [21], the experimental study in [20] started with two spectral estimators.
- The periodogram with a 4096-point fast Fourier transform (FFT).
- Tapered version of the same periodogram, using a Hamming window. With line components featuring prominently in the dataset, the experimental study also included two eigendecomposition-based spectral estimators: the multiple signal classification (MUSIC) algorithm [22], and the modified forward–backward linear prediction (MFBLP) algorithm [23].

The two classical spectral estimators failed in resolving the line components and also failed in correctly estimating the continuous parts of Marple's synthetic spectrum. On the other hand, the two eigendecomposition-based algorithms appeared to resolve the line components reasonably well but failed completely to correctly estimate the continuous parts of the spectrum.

Next, the MTM formula of (3) was tested with Marple's synthetic data, using a time–bandwidth product $C_o = 4$ and $K = 8$ Slepian tapers. The resulting composite spectrum appeared to estimate the continuous parts of the synthetic spectrum reasonably well and correctly identify the locations of the line components at −0.15 and 0.1, but lumped the line components at 0.2 and 0.21 into a composite combination around 0.21. With additional complexity through the inclusion of the *harmonic F-test for line components*, the composite spectrum computed by the MTM did reproduce the synthetic spectrum fully and accurately; the *F*-test is discussed in Section VII.

In light of the experimental results of [19] and [20] summarized herein, it can be said that the basic formula of the MTM in (3) did outperform the periodogram and its Hamming-tapered version, which is not surprising. Moreover, it outperformed the MUSIC and MFBLP algorithms insofar as the continuous parts of the spectrum are concerned but did not perform as well in dealing with the line components. However, when the composite MTM spectrum was expanded to include the *F*-test for line

components, Marple's synthetic spectrum was reconstructed fully and accurately.

It is also noteworthy that in [19] and [20], a comparative evaluation of the MTM and the traditional *maximum-likelihood parameter-estimation procedure,* known for its optimality, is presented for angle-of-arrival estimation in the presence of multipath using real-life radar data. The results presented therein for low-grazing angles show that these two methods are close in performance.

In another comparative study [24], Bronez compared the MTM with WOSA, which was originally proposed by Welch [17]. To make this comparison, theoretical measures were derived by Bronez in terms of leakage, variance, and resolution. The comparison was performed by evaluating each one of these three measures in turn while keeping the other two measures unchanged. The results of the comparison demonstrated that the MTM always performed better than WOSA. For example, given the same variance and resolution, it was found that the MTM had an advantage of 10–20 dB over WOSA.

IV. SPACE–TIME PROCESSING

As already discussed, the MTM is theorized to provide a reliable and accurate method of estimating the power spectrum of RF stimuli as a function of frequency. As such, in the MTM, we have a desirable method for identifying spectrum holes and estimating their average-power contents. In analyzing the radio scene in the local neighborhood of a cognitive radio receiver, however, we also need to have a *sense of direction,* so that the cognitive radio is able to *listen* to incoming interfering signals from unknown directions. What we are signifying here is the need for space–time processing. To this end, we may employ a set of sensors to properly "sniff" the RF environment along different directions.

To elaborate on this matter, consider an array of M antennas sensing the environment. For the kth Slepian taper, let $X_k^{(m)}(f)$ denote the complex-valued Fourier transform of the input signal $x(t)$ computed by the mth sensor in accordance with (1) and $m = 0, 1, \ldots, M - 1$. With $k = 0, 1, \ldots, K - 1$, we may then construct the M-by-K spatiotemporal complex-valued matrix

$$\mathbf{A}(f) = \begin{bmatrix} a_0^{(0)} X_0^{(0)} & a_1^{(0)} X_1^{(0)} & \cdots & a_{K-1}^{(0)} X_{K-1}^{(0)} \\ a_0^{(1)} X_0^{(1)} & a_1^{(1)} X_1^{(1)} & \cdots & a_{K-1}^{(1)} X_{K-1}^{(1)} \\ \vdots & \vdots & & \\ a_0^{(M-1)} X_0^{(M-1)} & a_1^{(M-1)} X_1^{(M-1)} & \cdots & a_{K-1}^{(M-1)} X_{K-1}^{(M-1)} \end{bmatrix} \tag{13}$$

where each row of the matrix is produced by RF stimuli sensed at a different gridpoint, each column is computed using a different Slepian taper, and the $a_k^{(m)}$ represent coefficients accounting for different areas of the gridpoints.

To proceed further, we make two necessary assumptions.

1) The number of Slepian tapers K is larger than the number of sensors M; this requirement is needed to avoid "spatial undersampling" of the RF environment.

2) Except for being synchronously sampled, the M sensors operate independently of each other; this second requirement is needed to ensure that the rank of the matrix $\mathbf{A}(f)$ (i.e., the number of linearly independent rows) is equal to M.

In physical terms, each entry in the matrix $\mathbf{A}(f)$ is produced by two contributions: one due to additive ambient noise at the front end of the sensor and the other due to the incoming RF stimuli. However, as far as spectrum sensing is concerned, the primary contribution of interest is that due to RF stimuli. In this context, an effective tool for denoising is the *singular value decomposition* (SVD).

The SVD is a generalization of principal-components analysis or eigendecomposition. Whereas eigendecomposition involves a single orthonormal matrix, the SVD involves a pair of orthonormal matrices, which we denote by an M-by-M matrix $\mathbf{U}$ and a K-by-K matrix $\mathbf{V}$. Thus, applying the SVD to the spatiotemporal matrix $\mathbf{A}(f)$, we may express the resulting decomposition as follows [25]:

$$\mathbf{U}^\dagger(f)\mathbf{A}(f)\mathbf{V}(f) = \begin{bmatrix} \mathbf{\Sigma}(f) \\ \text{----} \\ \mathbf{0} \end{bmatrix} \tag{14}$$

where the superscript $\dagger$ denotes *Hermitian transposition* and $\mathbf{\Sigma}(f)$ is an M-by-M diagonal matrix, the kth element of which is denoted by $\sigma_k(f)$. Fig. 1 shows an insightful depiction of this decomposition; to simplify the depiction, dependence on the frequency f has been ignored.

Henceforth, the system described by the spatiotemporal matrix $\mathbf{A}(f)$ of (13), involving K Slepian tapers, M sensors, and decomposition of the matrix in (14), is referred to as the *MTM-SVD processor*. Note that with the spatiotemporal matrix $\mathbf{A}(f)$ being frequency-dependent, and likewise for the unitary matrices $\mathbf{U}(f)$ and $\mathbf{V}(f)$, the MTM-SVD processor is actually performing *tensor analysis*.
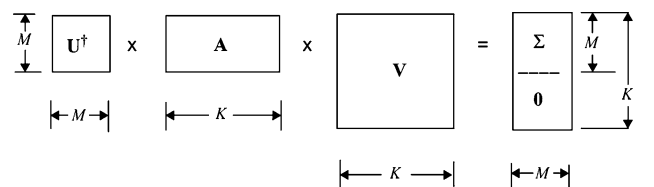

Fig. 1. *Diagrammatic depiction of singular value decomposition applied to the matrix A of (13).*

A. Physical Interpretation of the Action Performed by the MTM-SVD Processor

To understand the underlying signal operations embodied in the MTM-SVD processor, we begin by reminding ourselves of the orthonormal properties of matrices $\mathbf{U}$ and $\mathbf{V}$ that hold for all f, as shown by

$$\mathbf{U}(f)\mathbf{U}^{\dagger}(f) = \mathbf{I}_M$$

and

$$\mathbf{V}(f)\mathbf{V}^{\dagger}(f) = \mathbf{I}_K$$

where $\mathbf{I}_K$ and $\mathbf{I}_M$ are K-by-K and M-by-M identity matrices, respectively. Using this pair of relations in (14), we obtain the following decomposition of the matrix $\mathbf{A}(f)$ (after some straightforward manipulations):

$$\mathbf{A}(f) = \sum_{m=0}^{M-1} \boldsymbol{\sigma}_m \mathbf{u}_m \mathbf{v}_m^{\dagger}. \qquad (15)$$

The $\boldsymbol{\sigma}_m(f)$ is called the mth *singular value* of the matrix $\mathbf{A}(f)$, $\mathbf{u}_m(f)$ is called the *left-singular vector,* and $\mathbf{v}_m(f)$ is called the *right-singular vector*. In analogy with principal-components analysis, the decomposition of (15) may be viewed as one of the principal modulations produced by the incoming RF stimuli [2], [3], [26]. According to this decomposition, the singular value $\boldsymbol{\sigma}_m(f)$ scales the mth principal modulation computed by the MTM-SVD processor.

The M singular values, constituting the diagonal matrix $\boldsymbol{\Sigma}(f)$ in (14), are all real numbers. The higher order singular values, namely, $\boldsymbol{\sigma}_M(f), \ldots, \boldsymbol{\sigma}_{K-1}(f)$, are all zero; they constitute the null matrix $\mathbf{0}$ in (14).

Using (15) to form the matrix product $\mathbf{A}(f)\mathbf{A}^{\dagger}(f)$, and invoking the orthonormal property of the unitary matrix $\mathbf{V}(f)$, we have the eigendecomposition

$$\mathbf{A}(f)\mathbf{A}^{\dagger}(f) = \sum_{m=0}^{M-1} \boldsymbol{\sigma}_m^2(f)\mathbf{u}_m(f)\mathbf{u}_m^{\dagger}(f)$$

where $\boldsymbol{\sigma}_M^2(f)$ is the mth eigenvalue of the eigendecomposition. Similarly, forming the other matrix product $\mathbf{A}^{\dagger}(f)\mathbf{A}(f)$ and invoking the orthonormal property of the unitary matrix $\mathbf{U}(f)$, we have the alternative eigendecomposition

$$\mathbf{A}^{\dagger}(f)\mathbf{A}(f) = \sum_{k=0}^{M-1} \boldsymbol{\sigma}_k^2(f)\mathbf{v}_k(f)\mathbf{v}_k^{\dagger}(f)$$

where the eigenvalues for $k = M, \ldots, K-1$ are all zero.

Recalling that the index m signifies a sensor and the index k signifies a Slepian taper, we may now make three statements on the multiple operations being performed by the MTM-SVD processor.

1) The mth eigenvalue $\boldsymbol{\sigma}_m^2(f)$ is defined by

$$\boldsymbol{\sigma}_m^2(f) = \sum_{k=0}^{K-1} \left| a_k^{(m)}(f) \right|^2 \left| X_k^{(m)}(f) \right|^2.$$

Setting $|a_k^{(m)}(f)|^2 = \lambda_k^{(m)}(f)$ and dividing $\boldsymbol{\sigma}_m^2(f)$ by $\sum_{k=0}^{K-1} \lambda_k^{(m)}(f)$, we get

$$\hat{S}^{(m)}(f) = \frac{\sum_{k=0}^{K-1} \lambda_k^{(m)}(f) \left| X_k^{(m)}(f) \right|^2}{\sum_{k=0}^{K-1} \lambda_k^{(m)}(f)},$$
$$m = 0, 1, \ldots, M-1 \quad (16)$$

which is a rewrite of (3), specialized for sensor m. We may therefore make the following statement:

The eigenvalue $\boldsymbol{\sigma}_m^2(f)$, except for the scaling factor $\sum_{k=0}^{K-1} \lambda_k^{(m)}(f)$, provides the desired multitaper spectral estimate of the incoming interfering signal picked up by the mth sensor.

2) Since the index m refers to the mth sensor, we make the following second statement:

The left singular vector $\mathbf{u}_m(f)$ defines the direction of the interfering signal picked up by the mth sensor at frequency f.

3) The index k refers to the kth Slepian taper; moreover, since $\boldsymbol{\sigma}_k^2(f) = \boldsymbol{\sigma}_m^2(f)$ for $k = 0, 1, \ldots, M-1$, we may make the third and last statement:

The right singular vector $\mathbf{v}_m(f)$ defines the multitaper coefficients for the mth interferer's waveform.

Most importantly, with no statistical assumptions on the additive ambient noise in each sensor or the incoming RF interferers, we may go on to state that the nonparametric MTM-SVD processor is indeed *robust*.

The enhanced signal-processing capability of the MTM-SVD processor just described is achieved at the expense of increased computational complexity. To elaborate, with N data points and signal bandwidth $2W$, there are N different frequencies with spectral resolution $2W$ to be considered. Accordingly, the MTM-SVD processor has to perform a total of N singular value decompositions on matrix $\mathbf{A}(f)$. Note, however, that the size of the wavenumber spectrum (i.e., the spatial distribution of the

interferers) is determined by the number of sensors M, which is considerably smaller than the number of data points N. Most importantly, the wavenumber is computed in *parallel*. With the computation being performed at each frequency f, each of the M sensors sees the full spectral footprint of the interferer pointing along its own direction; the footprint is made up of N frequency points with a spectral resolution of $2W/N$.

Summing up, the MTM-SVD processor has the capability to sense the surrounding RF environment both in frequency as well as space, the resolutions of which are respectively determined by the number of data points and the number of sensors deployed.

V. TIME–FREQUENCY ANALYSIS

The MTM-SVD processor rests its signal-processing capability on two dimensions of sensing:

- *frequency,* which is necessary for identifying the location of spectrum holes along the frequency axis;
- *space,* which provides the means for estimating wavenumber spectra of the RF environments.

However, for a cognitive radio to be fully equipped to sense its local neighborhood, there is a third dimension of sensing that is just as important: *time*. The inclusion of time is needed for the cognitive radio receiver to sense the type of modulation employed by the primary user, for example, so as to provide for a harmonious relationship with the primary user if, and when, it is needed. This need calls for time–frequency analysis.

The statistical analysis of nonstationary signals has had a rather mixed history. Although the general second-order theory was published during 1946 by Loève [27], [28], it has not been applied nearly as extensively as the theory of stationary processes published only slightly earlier by Wiener and Kolmogorov. There were, at least, four distinct reasons for this neglect, as summarized in [29].

i) Loève's theory was *probabilistic,* not statistical, and there does not appear to have been successful attempts to find a statistical version of the theory until some time later.

ii) At that time of publication, more than six decades ago, the mathematical training of most engineers and physicists in signals and stochastic processes was minimal. Recalling that even Wiener's delightful book was referred to as "the yellow peril" because of the color of its cover, it is easy to imagine the reception that a general nonstationary theory would have received.

iii) Even if the theory had been commonly understood at the time and good statistical estimation procedures had been available, the computational burden would probably have been overwhelming. This was the era when Blackman–Tukey estimates of the stationary spectrum were developed, not

because they were great estimates but, primarily, because they were simple to understand in mathematical terms and, before the (re)invention of the FFT algorithm, computationally more efficient than other forms.

iv) Lastly, it cannot be denied that the Loève theory of nonstationary processes was harder to grasp than that of stationary processes.

In any event, confronted with the notoriously unreliable nature of a wireless channel, we have to find some way to account for the nonstationary behavior of a signal at the channel output, and therefore *time* (implicitly or explicitly), in a description of the signal picked up by the receiver. Given the desirability of working in the frequency domain for well-established reasons, we may include the effect of time by adopting a time–frequency description of the signal. During the last three decades, many papers have been published on various estimates of time–frequency distributions; see, for example, Cohen's book [30] and the references therein. In most of this work, the signal is assumed to be *deterministic*. In addition, many of the proposed estimators are constrained to match time and frequency *marginal* density conditions. For a continuous-time signal $x(t)$, the *time marginal* is required to satisfy the condition

$$\int_{-\infty}^{\infty} D(t,f)\mathrm{d}f = |x(t)|^2 \tag{17}$$

where $D(t,f)$ is the time–frequency distribution of the signal. Similarly, if $X(f)$ is the Fourier transform of $x(t)$, the *frequency marginal* must satisfy the second condition

$$\int_{-\infty}^{\infty} D(t,f)\mathrm{d}t = |X(f)|^2. \tag{18}$$

Given the large differences observed between waveforms collected on sensors spaced short distances apart, the time marginal requirement is a rather strange assumption. Worse, the frequency marginal is, except for a factor of $1/N$, just the periodogram of the signal. It has been known, well before the first periodogram was computed [31], that the periodogram is badly biased and inconsistent.[2] Thus, we do not consider matching marginal distributions, as commonly defined in the literature, to be important.

---

[2]An *inconsistent estimate* is one where the variance of the estimate does not decrease with sample size. Rayleigh did not use the term "inconsistent" because it was not introduced as a statistical term until Fisher's famous paper nearly 30 years later.

A. Theoretical Background on Nonstationarity

Nonstationarity is an inherent characteristic of most, if not all, of the stochastic processes encountered in practice. Yet, despite its highly pervasive nature and practical importance, not enough attention is paid in the literature to the characterization of nonstationary processes in a mathematically satisfactory manner.

To this end, consider a complex continuous stochastic process, a sample function of which is denoted by $x(t)$, where t denotes continuous time. We assume that the process is harmonizable [27], [28], so that it permits the *Cramér representation*

$$x(t) = \int_{-1/2}^{1/2} \exp(j2\pi\nu t)dZ_x(\nu) \qquad (19)$$

where $dZ_x(\nu)$ is now an *increment process* associated with $x(t)$; the dummy variable ν has the same dimension as frequency. The bandwidth of $x(t)$ has been normalized to *unity* for convenience of presentation; consequently, as indicated in (19), the integration extends with respect to ν over the interval $[-1/2, +1/2]$. As before, it is assumed that the processor has zero mean, that is, $\mathbf{E}[x(t)] = 0$ for all time t; correspondingly, we have $\mathbf{E}[Z_x(\nu)] = 0$ for all ν. [Equation (19) is also the starting point in formulating the MTM.]

To set the stage for introducing the statistical parameters of interest, we define the covariance function

$$\begin{aligned}
\Gamma_L(t_1, t_2) &= \mathbf{E}\{x(t_1)x^*(t_2)\} \\
&= \int_{-\infty}^{\infty} \int_{-\infty}^{\infty} \exp(j2\pi(t_1 f_1 - t_2 f_2)) \\
&\quad \times \gamma_L(f_1, f_2)df_1 df_2
\end{aligned} \qquad (20)$$

where, in the first line, the asterisk denotes complex conjugation. Hereafter, the generalized two-frequency spectrum $\gamma_L(f_1, f_2)$ in the integrand of the second line in (20) is referred to as the *Loève spectrum*. With $X(f)$ denoting the Fourier transform of $x(t)$, the Loève spectrum[3] is formally defined as follows:

$$\gamma_L(f_1, f_2)df_1 df_2 = \mathbf{E}\left[dZ_x(f_1)dZ_x^*(f_2)\right] \qquad (21)$$

---

[3]Care should be exercised in distinguishing the Loève spectrum $\gamma_L(f_1, f_2)$ from the bispectrum $B(f_1, f_2)$. Both are functions of two frequencies, but the Loève spectrum $\gamma_L(f_1, f_2)$ is a *second*-moment description of a possibly nonstationary process; in contrast, the bispectrum describes the *third*-moments of a stationary process and has an implicit third frequency $f_3 = f_1 + f_2$.

where $dZ_x(f)$ is now an increment associated with $x(t)$. Equation (21) highlights the underlying feature of a nonstationary process by describing the *correlation* between the spectral elements $X(f_1)$ and $X(f_2)$ of the process at two different frequencies f_1 and f_2, respectively.

If the process is stationary, then by definition, the covariance $\Gamma_L(t_1, t_2)$ depends only on the time difference $t_1 - t_2$, and the Loève spectrum becomes $\delta(f_1 - f_2)S(f_1)$, where $\delta(f)$ is the Dirac delta function in the frequency domain and $S(f)$ is the ordinary power spectrum. Similarly, for a white nonstationary process, the covariance function becomes $\delta(t_1 - t_2)P(t_1)$, where $\delta(t)$ is the Dirac delta function in the time domain and $P(t)$ is the expected (average) power of the process at time t. Thus, as both the spectrum and covariance functions include delta-function discontinuities in simple cases, neither should be expected to be "smooth"; and *continuity properties* of the process therefore depend on direction in the (f_1, f_2) or (t_1, t_2) plane. The continuity problems are more easily dealt with by rotating both the time and frequency coordinates of the covariance function (20) and Loève spectrum (21), respectively, by 45°. In the time domain, we may now define the new coordinates to be a "center" t_0 and a delay τ, as shown by

$$\begin{aligned}
t_1 + t_2 &= 2t_0 \\
t_1 - t_2 &= \tau.
\end{aligned} \qquad (22)$$

Correspondingly, we may write

$$\begin{aligned}
t_1 &= t_0 + \tau/2 \\
t_2 &= t_0 - \tau/2.
\end{aligned} \qquad (23)$$

Thus, denoting the new covariance function in the *rotated coordinates* by $\Gamma(\tau, \tau_0)$, we may go on to write

$$\Gamma_L(t_1, t_2) = \Gamma(\tau, t_0). \qquad (24)$$

Similarly, we may define new frequency coordinates f and g by writing

$$\begin{aligned}
f_1 + f_2 &= 2f \\
f_1 - f_2 &= g.
\end{aligned} \qquad (25)$$

Correspondingly, we have

$$\begin{aligned}
f_1 &= f + g/2 \\
f_2 &= f - g/2.
\end{aligned} \qquad (26)$$

The *rotated two-frequency spectrum* is thus defined by

$$\gamma(f, g) = \gamma_L(f + g/2, f - g/2). \tag{27}$$

Substituting the definitions of (26) into (20) shows that the term $(t_1 f_1 - t_2 f_2)$ in the exponent of the Fourier transform becomes $t_0 g + \tau f$; hence, we have

$$\Gamma(\tau, t_0) = \int\limits_{-\infty}^{\infty} \left\{ \int\limits_{-\infty}^{\infty} \exp(j2\pi(\tau f + t_0 g)) \right\} \gamma(f, g) df dg. \tag{28}$$

In view of the principle of duality that embodies the inverse relationship between time and frequency (an inherent characteristic of Fourier transformation), the frequency f is associated with the time difference τ; accordingly, f corresponds to the ordinary frequency of stationary processes; we may therefore refer to f as the "stationary" frequency. Similarly, the frequency g is associated with the average time t_0; therefore, it describes the behavior of the spectrum over long time spans; hence, we refer to g as the "nonstationary" frequency.

Consider next the continuity of the *generalized spectral density* γ, reformulated as a function of f and g. On the line $g = 0$, the generalized spectral density γ is just the ordinary spectrum with the usual continuity (or lack thereof) conditions normally applying to stationary spectra. As a function of g, however, we expect to find a δ-function discontinuity at $g = 0$ if, for no other reason, almost all data contain some stationary additive noise. Consequently, smoothers in the (f, g) plane or, equivalently, the (f_1, f_2) plane should not be isotropic but require much higher resolution along the nonstationary frequency coordinate g than along the stationary frequency axis f.

A slightly less arbitrary way of handling the g coordinate is to apply the inverse Fourier transform to $\gamma(f, g)$ with respect to the nonstationary frequency g, obtaining [32]

$$D(t_0, f) = \int\limits_{-\infty}^{\infty} \exp(j2\pi t_0 g) \gamma(f, g) dg \tag{29}$$

as the *dynamic spectrum* of the process; the $D(t_0, f)$ in (29) is not to be confused with the time–frequency distribution in (17) and (18). The motivation behind (29) is to transform very rapid variations expected around $g = 0$ into

a slowly varying function of t_0 while, at the same time, leaving the usual dependence on f intact. From Fourier transform theory, we know that the Dirac delta function in the frequency domain is transformed into a constant in the time domain. It follows, therefore, that, in a stationary process, $D(t_0, f)$ does not depend on t_0 and assumes the simple form $S(f)$. Thus, we may invoke the Fourier transform to redefine the dynamic spectrum as

$$D(t_0, f) = \int\limits_{-\infty}^{\infty} \exp(-j2\pi\tau f)$$
$$\times \mathbf{E}\left\{ x\left(t_0 + \frac{\tau}{2}\right) x^*\left(t_0 - \frac{\tau}{2}\right) \right\} d\tau \tag{30}$$

where the expectation, or ensemble averaging, is performed on $x(t)$ for prescribed values of time t_0 and frequency f.

B. Spectral Coherences of Nonstationary Processes Based on the Loève Transform

From an engineering perspective, we usually like to have estimates of second-order statistics of the underlying physics responsible for the generation of a nonstationary process. Moreover, it would be desirable to compute the estimates using the multitaper method. With this twofold objective in mind, let $X_k(f_1)$ and $X_k(f_2)$ denote the multitaper Fourier transforms of the sample function $x(t)$; these two estimates are based on the kth Slepian taper and are defined at two different frequencies f_1 and f_2, in accordance with (1). To evaluate the *spectral correlation* of the process at f_1 and f_2, the traditional formulation is to consider the product $X_k(f_1)X_k^*(f_2)$ where, as before, the asterisk in $X_k^*(f_2)$ denotes complex conjugation. Unfortunately, we often find that such a formulation is *insufficient* in capturing the underlying second-order statistics of the process, particularly so in the case of several communication signals that are of interest in cognitive-radio applications.[4] To complete the second-order statistical characterization of the process, we need to consider products of the form $X_k(f_1)X_k(f_2)$, which do *not* involve the use of complex conjugation. However, in the literature on stochastic processes, statistical parameters involving products like $X_k(f_1)X_k(f_2)$ are frequently not named and therefore hardly used; and when they are used, not only are different terminologies

---

[4]For most complex-valued signals, the expectation $\mathbf{E}[x(t_1)x(t_2)]$, and therefore $\mathbf{E}[X(f_1)X(f_2)]$, is zero. For communication signals, however, this expectation is often not zero; examples of signals for which this statement holds include the ATSC-DTV signal, binary phase-shift keying, minimum-shift keying, offset QPSK, orthogonal frequency-division multiplexing, and Gaussian minimum-shift keying used in GSM wireless communications [33].

adopted but also some of the terminologies are misleading.[5]

To put matters right, in this paper we follow the terminology first described in a 1973 paper by Moores [35] and use the subscripts *inner* and *outer* to distinguish between spectral correlations based on products involving such terms as $X_k(f_1)X_k^*(f_2)$ and $X_k(f_1)X_k(f_2)$, respectively. Hereafter, estimates of spectral correlations so defined are referred to as estimates of the *first* and *second kinds*, respectively, and likewise for related matters.

With the matter of terminology settled, taking the complex demodulates of a nonstationary process at two different frequencies f_1 and f_2, and invoking the inherent orthogonality property of Slepian sequences, we may now formally define the estimate of the Loève spectrum of the first kind as

$$\hat{\gamma}_{L,\text{inner}}(f_1, f_2) = \frac{1}{K}\sum_{k=0}^{K-1} X_k(f_1)X_k^*(f_2) \tag{31}$$

where, as before, K is the total number of Slepian tapers. The estimate of the Loève spectrum of the second kind is correspondingly defined as

$$\hat{\gamma}_{L,\text{outer}}(f_1, f_2) = \frac{1}{K}\sum_{k=0}^{K-1} X_k(f_1)X_k(f_2). \tag{32}$$

Thus, given a stochastic process with the complex demodulates $X_k(f_1)$ and $X_k(f_2)$, the Loève spectral coherences of the first and second kinds are, respectively, defined as

$$C_{\text{inner}}(f_1, f_2) = \frac{\hat{\gamma}_{L,\text{inner}}(f_1, f_2)}{\left(\hat{S}(f_1)\hat{S}(f_2)\right)^{1/2}} \tag{33}$$

---

[5]In a terminological context, there is confusion in how second-order moments of complex-valued stochastic processes are defined in the literature: • Thomson [8] and Picinbono [34] use the terms forward and reversed to distinguish, for example, the second-order moments $\mathbf{E}[X_k(f_1)X_k^*(f_2)]$ and $\mathbf{E}[X_k(f_1)X_k(f_2)]$, respectively. In [35], Moores applies spectral analysis to physical-oceanographic data, in the context of which two kinds of cross-correlation functions for a pair of complex-valued time series $x_j(t)$ and $x_k(t)$ are introduced. 1) The inner cross-correlation function is defined by the expectation $\mathbf{E}\{x_j^*(t)x_k(t+\tau)\}$ for some τ, where the asterisk denotes complex conjugation; this second-order moment is so called because it resembles an inner product. 2) The outer cross-correlation function is defined by the expectation $\mathbf{E}\{x_j(t)x_k(t+\tau)\}$, where there is no complex conjugation; this alternative second-order moment is so called because it resembles an outer product. In the cyclostationarity literature on communication signals, the terms spectral correlation and conjugate spectral correlation are used to refer to the expectation $\mathbf{E}[X_k(f_1)X_k^*(f_2)]$ and $\mathbf{E}[X_k(f_1)X_k(f_2)]$, respectively. This terminology is misleading: if $\mathbf{E}[X_k(f_1)X_k^*(f_2)]$ stands for spectral correlation, then the expression for conjugate spectral correlation would be $\mathbf{E}[X_k^*(f_1)X_k(f_2)]$, which is not the intention. As stated in the text, this paper follows Moores' terminology.

and

$$C_{\text{outer}}(f_1, f_2) = \frac{\hat{\gamma}_{L,\text{outer}}(f_1, f_2)}{\left(\hat{S}(f_1)\hat{S}(f_2)\right)^{1/2}}. \tag{34}$$

With the eigenvalue λ_k being real valued for all k and f, the multitaper spectral estimate $\hat{S}(f)$ in (3) is real valued, so it should be. In general, the Loève spectral coherences $C_{\text{inner}}(f_1, f_2)$ and $C_{\text{outer}}(f_1, f_2)$ are both complex valued, which means that each of them will have its own magnitude and associated phase. The magnitudes of both spectral coherences are invariant under coordinate rotation, which is equivalent to multiplying $x(t)$ by $\exp(j\theta)$, where the constant θ is the angle of rotation. On the other hand, the phases of the inner and outer spectral coherences are altered by different amounts. In practice, we find that a quantity called the *two-frequency magnitude-squared coherence* (TF-MSC) is more useful than the spectral coherence itself; this point will be demonstrated in Sections VII and VIII. With the two spectral coherences of (33) and (34) at hand, we have two TF-MSCs to consider, namely, $|C_{\text{inner}}(f_1, f_2)|^2$ and $|C_{\text{outer}}(f_1, f_2)|^2$, respectively.

C. Two Special Cases of the Dynamic Spectrum

1) Wiger–Ville Distribution: From the defining (30), we immediately recognize that

$$W(t_0, f) = \int_{-\infty}^{\infty} \exp(-j2\pi\tau f)x\left(t_0 + \frac{\tau}{2}\right)x^*\left(t_0 - \frac{\tau}{2}\right)d\tau \tag{35}$$

is the formula for the Wigner–Ville distribution of the original sample function $x(t)$. In other words, we see that the rotated Loève spectrum is the expected value of the Wigner–Ville distribution [29], [36]. Stated in another way, the Wigner–Ville distribution is the instantaneous estimate of the dynamic spectrum of the nonstationary signal $x(t)$ and, therefore, simpler to compute than $D(t_0, f)$ in the classification of signals; for example, see [29].

A cautionary note on the use of (35): the naive implementation of the Wigner–Ville distribution, as defined in this equation using a finite sample size, may result in bias and sampling properties that are worse than the periodogram. For an improved version of the Wigner–Ville distribution, see [37].

2) Cyclic Power Spectrum: The dynamic spectrum also embodies another special case, namely, the *cyclic power spectrum* of a sample function $x(t)$ that is known to be *periodic*. Let T_0 denote the period of $x(t)$. Then, replacing

the time t_0 in (30) with $T_0 + t$, we may express the time-varying power spectrum of $x(t)$ as

$$S_x(t,f) = \int_{-\infty}^{\infty} \exp(-j2\pi\tau f)\mathbf{E}\Big\{x\Big(t + T_0 + \frac{\tau}{2}\Big)x^*$$
$$\times\Big(t + T_0 - \frac{\tau}{2}\Big)\Big\}d\tau$$
$$= \int_{-\infty}^{\infty} \exp(-j2\pi\tau f)R_x\Big(t + T_0 + \frac{\tau}{2}, t + T_0 - \frac{\tau}{2}\Big)d\tau$$

(36)

where

$$R_x\Big(t + T_0 + \frac{\tau}{2}, t + T_0 - \frac{\tau}{2}\Big)$$
$$= \mathbf{E}\Big[x\Big(t + T_0 + \frac{\tau}{2}\Big)x^*\Big(t + T_0 - \frac{\tau}{2}\Big)\Big] \quad (37)$$

is the *time-varying autocorrelation function* of the signal $x(t)$. The stochastic process, represented by $x(t)$, is said to be cyclostationary in the second-order sense if this autocorrelation sequence is itself periodic with period T_0, as shown by

$$R_x\Big(t + T_0 + \frac{\tau}{2}, t + T_0 - \frac{\tau}{2}\Big) = R_x\Big(t + \frac{\tau}{2}, t - \frac{\tau}{2}\Big). \quad (38)$$

Under this condition, (36) reduces to

$$S_x(t,f) = \int_{-\infty}^{\infty} \exp(-j2\pi\tau f)R_x\Big(t + \frac{\tau}{2}, t - \frac{\tau}{2}\Big)d\tau \quad (39)$$

which, as expected, is independent of the period T_0. Equation (39) is recognized as the cyclostationary extension of the *Wiener–Khintchine relation* for stochastic processes.

To be more complete, for a stochastic process to be cyclostationary in the second-order sense, its mean must also be periodic with the same period T_0. When the mean of the stochastic process under study is zero for all time t, this condition is immediately satisfied.

D. Diagrammatic Instrumentation for Computing Loève Spectral Correlations

Before proceeding to discuss cyclostationarity characterization of nonstationary processes in the next section, we find it instructive to have a diagrammatic instrumen-

tation for computing the Loève spectral correlations using the multitaper method. To do this, we look to the defining (1), (31), and (32), where t in (1) denotes discrete time and f in all three equations denotes continuous frequency. Let $x(t)$ denote a time series of length N. Then, the inspection of (1), (31), and (32) leads to the *basic instrument* diagrammed in Fig. 2(a). In particular, in accordance with (1), the identical functional blocks labeled "multitaper method" in the upper and lower paths of the figure produce the Fourier transforms $X_k(f_1)$ and $X_k(f_2)$, respectively. The designation "basic" is intended to signify that the instrument applies to both kinds of the Loève spectral correlation, depending on how the cross-correlation of the Fourier transforms $X_T(f_1)$ and $X_T(f_2)$ is computed over the set of K Slepian tapers. To be specific, we say that as the overall output:

- the instrument computes the estimate $\hat{\gamma}_{L,\text{inner}}(f_1,f_2)$ of (31) if the cross-correlation is of the first kind;
- it computes $\hat{\gamma}_{L,\text{outer}}(f_1,f_2)$ of (32) if the cross-correlation is of the second kind.

Fig. 2(b) applies to spectral correlations rooted in the Fourier framework, considered in the next section.

VI. CYCLOSTATIONARITY: FOURIER PERSPECTIVE

When the issue of interest is the characterization of digital modulated signals in cognitive-radio applications, we find that there is a large body of literature on the subject, the study of which has been an active area of research for more than 50 years. In historical terms, the prominence of cyclostationarity for signal detection and classification[6] is attributed to the work of Gardner in the 1980s [39], [40] and the subsequent work of Giannakis on alternative views and applications of cyclostationarity [48]. The literature on cyclostationarity includes the recent book by Hurd and Miamee [49] and the bibliography due to Serpedin *et al.* [9] that lists more than 1500 papers on the subject.

A. Fourier Framework of Cyclic Statistics

As defined previously in Section V, a stochastic process represented by the sample function $x(t)$ is said to be cyclostationary in the second-order sense if its time-varying autocorrelation function $R_x(t + \tau/2, t - \tau/2)$ satisfies the

---

[6]Research interest in cyclostationarity for signal detection and classification has experienced a resurgence with the emergence of cognitive radio, resulting in a signal-detection technique in the draft form of the IEEE802.22 standard. It has also featured in other applications that include the following: • detection of cochannel and adjacent signals, which is a key property that can mitigate the hidden-node problem in cognitive radio [38]; discrimination between various types of modulation [39]–[41]; estimation of modulation parameters [42]; allowing a signal of interest to be distinguished without demodulating the signal [43]; identification of the transmission equipment that may have created a transmitted signal of interest [44]; supporting information for geolocation algorithms [45], adaptive temporal [46] and spatial interference rejection [47], which can further help the signal detection and classification process.
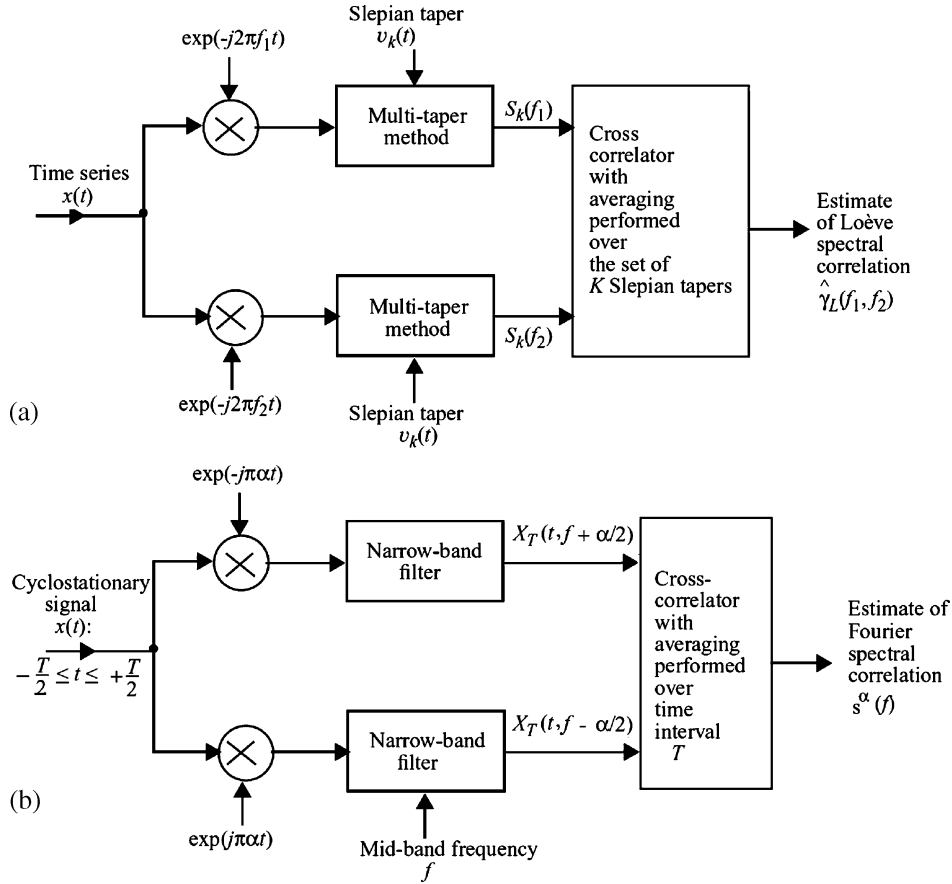
Fig. 2. *One-to-one correspondences between the Loève and Fourier theories for cyclostationarity. Basic instrument for estimating (a) the Loève spectral correlations of a time series x(t) and (b) the Fourier spectral correlations of cyclostationary signal x(t).*

periodicity condition of (38). Moreover, if the mean of the process is nonzero, it would also have to be time-varying with the same period T_0. For the present discussion, the mean is assumed to be zero for all time t, and attention is therefore focused on second-order statistics.

A cyclostationary process may also be described in terms of its power spectrum, which assumes a periodic form of its own. With interest in this paper focused on spectral coherence, we now go on to define the inner and outer forms of spectral coherence of a cyclostationary process using Fourier theory.

Let $x(t)$ denote a sample function of a complex-valued cyclostationary process with period T_0. Using the Fourier series, we may characterize the process by its cyclic power spectrum of the first kind, as shown by the Fourier expansion

$$S_{\text{inner}}(t,f) = \sum_\alpha s_{\text{inner}}^\alpha(f) \exp(j2\pi\alpha t) \qquad (40)$$

where the new parameter α, in theory, scans an infinite set of frequencies, namely, $n/T_0 = nf_0$, where $n = 0, 1, 2, \ldots$

The power spectrum of (40) is cyclic in that it satisfies the condition of periodicity

$$S_{\text{inner}}(t + T_0, f) = S_{\text{inner}}(t, f).$$

The Fourier coefficients in (40), namely, $s_{\text{inner}}^\alpha(f)$ for varying α, are defined by

$$s_{\text{inner}}^\alpha(f) = \lim_{T\to\infty} \lim_{\Delta t\to 0} \frac{1}{\Delta t}$$
$$\times \int_{-\Delta t/2}^{\Delta t/2} \frac{1}{T} X_T(t, f + \alpha/2) X_T^*(t, f - \alpha/2) dt. \quad (41)$$

The infinitesimally small Δt is included in (41) to realize the continuous-time nature of the cyclostationary signal $x(t)$ in the limit as Δt approaches zero. The

time-varying Fourier transform of $x(t)$, denoted by $X_T(t, f)$, is defined by

$$X_T(t, f) = \int_{t-T/2}^{t+T/2} x(\xi) \exp(-j2\pi f\xi) d\xi. \quad (42)$$

Most importantly, $s_{\text{inner}}^\alpha(f)$ is the time-average of the inner product $X_T(f + \alpha/2)X_T^*(f - \alpha/2)$; it follows, therefore, that $s_{\text{inner}}^\alpha(f)$ is the inner spectral correlation of the cyclostationary signal $x(t)$ for the two frequencies $f_1 = f + \alpha/2$ and $f_2 = f - \alpha/2$.

In light of the rationale presented in Section VI, we say that (40) and (41) provide a *partial description* of the second-order statistics of a complex-valued cyclostationary process. To complete the statistical description, we need to introduce the cyclic power spectrum of the second kind, as shown by

$$S_{\text{outer}}(t, f) = \sum_\alpha s_{\text{outer}}^\alpha(f) \exp(j2\pi\alpha t) \quad (43)$$

where $s_{\text{outer}}^\alpha(f)$ is the time average of the outer product $X_T(t, f + \alpha/2)X_T(t, f - \alpha/2)$, which does not involve the use of complex conjugation.

With (41) and (43) at hand, we may now define the two *Fourier spectral coherences* of a cyclostationary process as follows:

1) Fourier inner spectral coherence

$$C_{\text{inner}}^\alpha(f) = \frac{s_{\text{inner}}^\alpha(f)}{\left(s^0(f + \alpha/2)s^0(f - \alpha/2)\right)^{1/2}}. \quad (44)$$

2) Fourier outer spectral coherence

$$C_{\text{outer}}^\alpha(f) = \frac{s_{\text{outer}}^\alpha(f)}{\left(s^0(f + \alpha/2)s^0(f - \alpha/2)\right)^{1/2}}. \quad (45)$$

Both spectral coherences have the same denominator, where the Fourier coefficient $s^0(f)$ corresponds to $\alpha = 0$; putting $\alpha = 0$ in the expressions for $s_{\text{inner}}^\alpha(f)$ and $s_{\text{outer}}^\alpha(f)$ yields the common formula

$$s^0(f) = \lim_{T\to\infty} \lim_{\Delta t\to 0} \frac{1}{\Delta t} \int_{-\Delta t/2}^{\Delta t/2} \frac{1}{T} |X_T(t, f)|^2 dt. \quad (46)$$

As with the Loève spectral coherences, the Fourier spectral coherences are both complex-valued in general, with each of them having a magnitude and associated phase of its own.

The use of the Fourier spectral coherence of the first and second kinds in (44) and (45) can require excessive memory and can be computationally demanding in practice. To simplify matters, the *cycle frequency-domain profile* (CFDP) versions of spectral coherence is often used

$$\text{CFDP}_{\text{inner}}(\alpha) = \max_f \left| C_{\text{inner}}^\alpha(f) \right| \quad (47)$$

and similarly for the outer spectral coherence $C_{\text{outer}}^\alpha(f)$.

B. Diagrammatic Instrumentation for Computing the Fourier Spectral Correlations

The block diagram of Fig. 2(b) depicts the instrument [50] for computing the inner and outer kinds of the Fourier spectral correlations at frequencies $f_1 = f + \alpha/2$ and $f_2 = f - \alpha/2$ in accordance with (41) for $s_{\text{inner}}^\alpha(f)$ and its counterpart for $s_{\text{outer}}^\alpha(f)$. A cyclostationary signal $x(t)$ is applied in parallel to two paths, both of which use identical narrow-band filters. Both filters have the midband frequency f and bandwidth Δf, where the Δf is small compared with f but large enough compared with the reciprocal of the time T that spans the total duration of the input signal $x(t)$. In any event, the Fourier transform of the input $x(t)$ is shifted due to the multiplying factors $\exp(\pm j\pi\alpha t)$, producing the following filter outputs: $X_T(f + \alpha/2)$ in the upper path and $X_T(f - \alpha/2)$ in the lower path. Depending on how these two filter outputs are processed by the spectral correlator, the overall output is $s_{\text{inner}}^\alpha(f)$ or $s_{\text{outer}}^\alpha(f)$.

C. Relationship Between the Fourier and Loève Spectral Coherences

Much of the communications literature on cyclostationarity and related topics such as spectral coherence differ from that on multitaper spectral analysis. Nevertheless, these two approaches to cyclostationarity characterization of an input signal are related. In particular, examining parts Fig. 2(a) and (b), we see that the two basic instruments depicted therein are similar in signal-processing terms in that they exhibit the following one-to-one correspondences.

1) The multiplying factors $\exp(-j2\pi f_1 t)$ and $\exp(-j2\pi f_2 t)$ in Fig. 2(a) play similar frequency-shifting roles as the factors $\exp(j\pi\alpha t)$ and $\exp(-j\pi\alpha t)$ in Fig. 2(b).

2) The MTM in Fig. 2(a) for a prescribed Slepian taper and the narrow-band filter in Fig. 2(b) for prescribed midband frequency f and parameter α perform similar filtering operations.

3) Finally, the cross-correlator operates on the MTM outputs $X_k(f_1)$ and $X_k(f_2)$ in Fig. 2(a) to produce estimates of the Loève spectral correlations, while the cross-correlator in Fig. 2(b) operates on the filter outputs $X_T(t, f + \alpha/2)$ and $X_T(t, f - \alpha/2)$ to produce the Fourier spectral correlations with $f_1 = f + \alpha/2$ and $f_2 = f - \alpha/2$.

Naturally, the instruments depicted in Fig. 2(a) and 2(b) differ from each other by the ways in which their individual components are implemented.

D. Contrasting the Two Theories on Cyclostationarity

The theory of cyclostationarity presented in this section follows the framework originally formulated in Gardner [50]. This framework is rooted in the traditional Fourier transform theory of stationary processes with an important modification: introduction of the parameter α (having the same dimension as frequency) in the statistical characterization of cyclostationary processes. Accordingly, the cyclic spectral features computed from this formula depend on how well the parameter α matches the underlying statistical periodicity of the original signal $x(t)$.

The other theory on cyclostationarity, discussed previously in Section VI, follows the framework originally formulated in [32]. This latter framework combines the following two approaches:

- the Loève transform for dealing with nonstationary processes;
- the multitaper method for resolving the bias-variance dilemma through the use of Slepian sequences.

This two-pronged mathematically rigorous strategy for the time–frequency analysis of nonstationary processes has a *built-in* capability to adapt to the underlying statistical periodicity of the signal under study. In other words, it is nonparametric and therefore robust.

The Fourier-based approach to cyclostationarity may also acquire an adaptive capability of its own. In many spectrum-sensing applications based on this approach, the Fourier inner and outer spectral coherences, defined in (44) and (45), are computed over the entire spectral domain of interest, and the *actual* cycle frequencies (i.e., statistical periodicity of the signal) may thus be accurately estimated. According to Spooner [33], applicability of the Fourier-based cyclostationarity approach to spectrum sensing is thereby extended to a wide range of situations, ranging from completely blind (no prior knowledge of periodicity) to highly targeted (known periodicities with possible errors).

Summing up the basic similarities and differences between the Loève and Fourier theories of stochastic processes, we say the following.

- Both theories perform similar signal-processing operations on their inputs.

- The Fourier theory assumes that the stochastic process is cyclostationary, whereas the Loève theory applies to any nonstationary process regardless of whether it is cyclostationary.

E. Practical Considerations

In the use of cyclostationarity as a tool for signal detection and classification, there are several practical issues that may present challenges.

1) Communication systems have timing variations due to the imprecision of their clocks. In practice, this means that the signal is not truly cyclostationary, but it may be over some finite blocks of time. Long-duration averaging, however, tends to attenuate the spectral correlation feature when the time-varying clock randomizes the phase [51].

2) Channel effects such as Doppler shift and/or fading diminish the periodic nature of the signal phase-transitions (e.g., modulation), and thus can also reduce the practical extent of data collection [52].

3) Not all signals can be classified with second-order cyclostationarity. For example, there is an ambiguity between various forms of pulse-amplitude modulation in the cyclic spectrum [53]. This ambiguity can be overcome to some extent by exploiting higher order cyclostationarity, such as *cyclic cumulants,* but estimation of higher order moments is known to require substantially more data as well as complexity [54]. Note also that higher order moments are very sensitive to outliers such as impulsive noise.

4) For a given modulated signal $x(t)$, computing a three-dimensional surface defined by $|C_x^{(\alpha)}(f)|$ for varying α and f is computationally intensive. However, in practice, it may not be necessary to compute the entire surface if assumptions about the operating band can be made, thereby reducing the region of computation. Furthermore, some computationally reduced algorithms have been developed to deal with this difficulty [55].

5) If there are several signals in the environment, then some pattern-recognition techniques are necessary to identify and sort out the myriad of features to determine the combination of signals that created those features.

6) The final issue pertains to highly filtered signals. As the pulse-shaping becomes more aggressive to reduce bandwidth, cyclic features for many types of modulation tend to diminish, requiring even more data to be collected so as to reduce the variance of the cyclostationarity estimator to reveal weak features.

The issues described herein have been discussed in the literature in the context of the classical Fourier theory of cyclostationarity.

VII. FIRST EXAMPLE: WIDE-BAND ATSC DIGITAL TELEVISION SIGNAL

In cognitive-radio applications, the requirement is to make estimates of the average power of incoming RF stimuli *quickly*; hence, estimating the spectrum on short data blocks (each consisting of N samples) is a *priority*. Communication signals are designed not to waste power on unnecessary redundant components. Consequently, much of the cyclostationarity of the transmitted signal occurs because of framing, data blocks, etc., which may be separated by more than the fundamental period T_0, and so do not show up in short-data blocks. Simply put, reliable spectrum sensing for cognitive-radio applications is *complicated* not only by the many characteristics of wireless communication signals but also by interfering signals, fading, and noise, all of which make the task of spectrum sensing highly demanding.

A. Spectral Characteristics of the ATSC-DTV Signal

For our first experimental study, we consider the digital representation of wideband ATSC signals. The ATSC-DTV is an eight-level *vestigial sideband* (VSB) modulated signal used for terrestrial broadcasting that can deliver a Moving Picture Expert Group-2 Transport Stream (MPEG-2-TS) of up to 19.39 Mbits per second (Mbps) in a 6 MHz channel with 10.72 Msymbols per second (over-the-air medium); for more details, see Bretl *et al.* [56]. A pilot is inserted into the signal at 2.69 MHz below the center of the signal (i.e., one-quarter of the symbol rate from the signal center). Typically, there are also several other narrow-band signals found in the analysis bandwidth, thereby complicating the spectrum-sensing problem.

Using the MTM, we may generate a reasonable estimate of the available spectrum with about 100 μs of data. Spectra of such data are slightly less variable than a spectrum estimated from Gaussian data. If we compute Bartlett's M-test[7] as a function of frequency, we find that it is superstationary, in the sense that there is less variation from section to section than that expected in a stationary Gaussian process.

Fig. 3 shows the minimum, average, and maximum of 20 multitaper estimates of the ATSC-DTV power spectrum. Here, the block length used was N = 2200 samples, or 110 μs in duration. The blocks were offset 100% from each other. The pilot carrier is clear at the lower band-edge
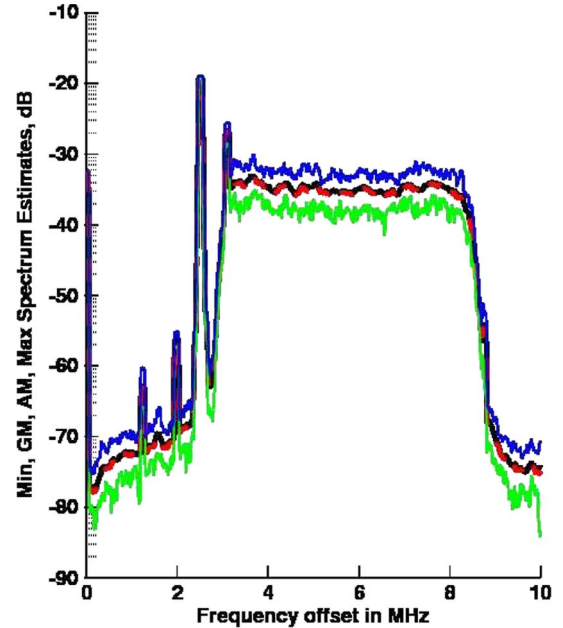

Fig. 3. *Multitaper estimates of the spectrum of the ATSC-DTV signal. Each estimate was made using $C_o = 6.5$ with K = 11 tapers. In this example, N = 2200, or 110 μs. The lower (green) and upper (blue) curves represent the minimum and maximum estimates over 20 sections.* Note: *When the figure is expanded sufficiently, we see two closely overlapping curves: the arithmetic (upper black) and geometric (lower blue) means.*

of the MTM spectrum. Clearly, there are considerable white spaces in the spectrum to fit in additional signals; hence the interest in the use of white spaces in the TV band for cognitive-radio applications.[8]

The ATSC-DTV signal is clearly seen to be 40 dB or more above the noise and the sharp narrow-band interfering components. (As a matter of practical interest, if the signal-to-noise ratio were lower, as in a wide-band signal, for example, then the classification would be more difficult and more subtle characteristics such as cyclostationarity would be necessary to distinguish between signals and noise.) Both below and above the main ATSC-DTV signal, the slowly varying shape of the baseline spectrum estimates is reminiscent of filter skirts, which makes it

---

[7]If we have J spectrum estimates, $S(f, j)$, $j = 1, \ldots, J$, with an average DoF of $\nu(f)$ from (12), Bartlett's M-test for homogeneity-of-variances is defined as follows [57], [58]:

$$M(f) = J\nu(f) \ln\left[\frac{A\{S(f,j)\}}{G\{S(f,j)\}}\right]$$

where $A\{S(f,j)\}$ and $G\{S(f,j)\}$ denote the arithmetic and geometric means of the J estimates at frequency f. This test is a likelihood-ratio test and approximately distributed as chi-squared χ^2_{J-1}. The M in Bartlett's M-test must not be confused with the symbol used to denote the number of sensors in Section IV.

[8]In its 2008 Report and Order on TV white space [11], the FCC established rules to allow new wireless devices to operate in the white space (unoccupied spectrum) of the broadcast television spectrum on a secondary basis. It is expected that this will lead to new innovative products, especially broadband applications. To avoid causing interference, the new devices will incorporate geolocation capability and the ability to access over the Internet a database of primary spectrum users, such as locations for TV stations and cable systems headends. The database itself is insufficient to offer interference guarantees, given the inability to accurately predict propagation characteristics while efficiently using the spectrum. The portability of low-power primary users, such as wireless microphones, makes the database approach infeasible, motivating the need for sensitive and accurate spectrum-sensing technology to include these devices.

improbable that the true thermal noise level is reached anywhere in this band.

Note also that, as anticipated, there are several *narrow-band interfering signals* visible in the MTM spectrum of Fig. 3:

- four strong signals (one nearly hidden by the vertical-axis) and three others on the low side;
- two weak signals: one at 1.6 MHz (maximum level of about −65 dB, about halfway between the peaks at 1.245 and 1.982 MHz), and one halfway down the upper skirt at 8.7 MHz.

If we were to use a conventional periodogram or its tapered (windowed) version to estimate the ATSC-DTV spectrum, then the presence of interfering narrow-band signals such as those in Fig. 3 would be obscured. Accordingly, in using the white spaces of the TV band, careful attention has to be given to the identification of interfering narrow-band signals.[9]

The ATSC-DTV signal is a useful example of how the naive use of Loève spectra can be misleading. Using (33) and (34) for the TF-MSC, Fig. 4 shows an estimate of the two-frequency coherence $|C(f_1, f_2)|^2$ that is made on the raw eigencoefficients. Here, the striking feature is the block of points in the range $0 < f_1, f_2 < 3.1$ MHz and points near 8.7 MHz on both axes, where the *minimum* coherence measured on 20 disjoint segments is between 20% and 75%. Note also the visibility of the interfering signals is clearer in Fig. 3, where they are responsible for the high coherence points on the misleading estimate.

Under the null hypothesis, the significance of minimum coherence is much higher for a given level than it is for the TF-coherences on single sections. For a single multitaper coherence estimate, the probability density function of a single MSC estimate, denoted by q, when the true coherence is zero is [18]

$$p(q) = (K-1)(1-q)^{K-2} \qquad (48)$$

where K is the number of Slepian tapers. Correspondingly, the cumulative distribution function of the estimate q is

$$P(q) = 1 - (1-q)^{K-1}. \qquad (49)$$

If we take the minimum of J such independent estimates, standard results for order statistics show that the distribution is of the same form as (49) but with an

Fig. 4. *A misleading estimate of the two-frequency magnitude-squared coherence $|C(f_1, f_2)|^2$ for the ATSC-DTV signal. The plot is split, showing inner coherences in the upper left-half and outer coherences in the lower-right half. The plotted coherences represent the minimum coherence over 20 disjoint segments. The estimates were made using $C_o = 6.5$, $K = 11$, and $N = 2200$. The pattern of high values in the lower left could be easily mistaken for cyclostationarity, but it is almost completely an artifact of the strong carriers below the ATSC-DTV band-edge.*

equivalent K, defined $K_e = J(K-1) + 1$; for example, see [59, Ch. 14]. Specifically

$$P\{\min(q_1, \ldots, q_J) \geq q\} = (1-q)^{J(K-1)}. \qquad (50)$$

Taking $K = 8$, the median TF-MSC is approximately 0.09438, and the 90% level is at 0.2803. The probability that the minimum of five such estimates exceeds the threshold 0.2803 is about 10^{-5}. If the dataset is stationary, taking the minimum of J estimates is less efficient than estimating the coherences from all $J \times K$ eigencoefficients. There are good reasons for why the minimum coherence may be preferred to the full estimate.

i) The minimum TF-MSC is preferred over the standard estimate when speed of computation is an issue of practical concern. The advantage of using the minimum TF-MSC is particularly marked when a running estimate over the last J blocks is kept.

ii) When the power is varying, the minimum coherence may be more reliable than the standard estimate. For two series, say, $\{x\}$ and $\{y\}$, and K eigencoefficients on J different time-blocks, denote the respective eigencoefficients as $x_k(j, f)$ and $y_k(j, f)$. An estimate of the coherence averaged over both windows and blocks is optimum when

---

[9]The IEEE 802.22 Web site https:mentor.ieee.org/802.2/file/07/22-07-0341-00-001-improved-fec-features.doc avoids a spectrum-sensing scheme using *pilot detection*. Indeed, the location of the pilot in the TV band is well defined; hence detection of the pilot itself can be done reliably. However, recognizing the practical inevitability of finding interfering narrow-band signals below the pilot, as demonstrated in the MTM spectrum of Fig. 3, undermines the practicality of the pilot-detection approach.
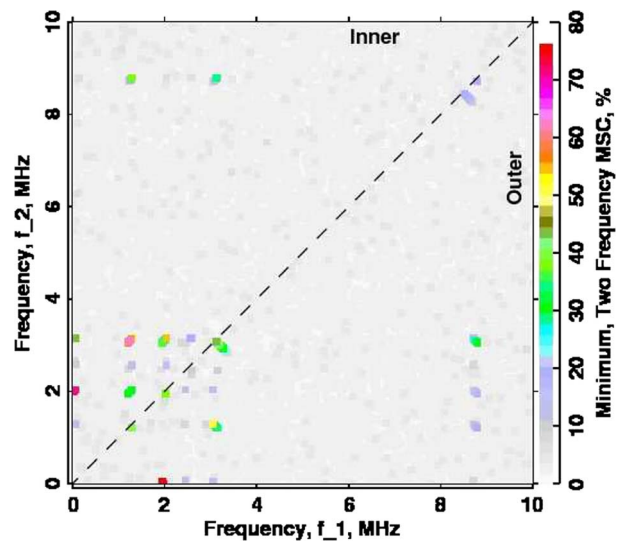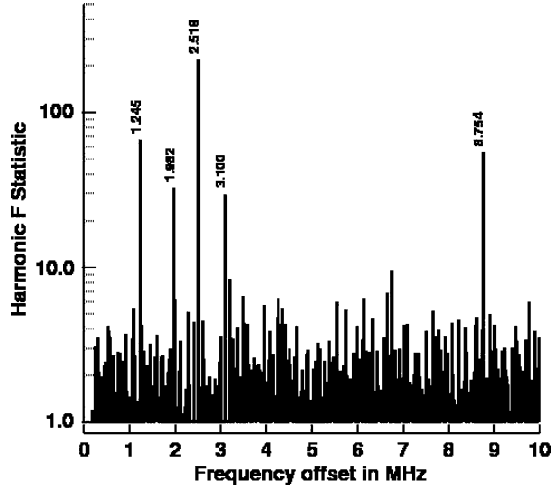
Fig. 5. *Harmonic-F test for periodic components in the ATSC-DTV signal. The test has two and 20 degrees of freedom, and the threshold level was set at the 99.9% significance level. Note the symmetric pair of sidebands on the signal at 2.518 MHz that appears visually broadened in the spectrum shown in Fig. 4; similarly for the line at 8.754 MHz that appears as a small "bump" on the upper skirt of the main signal.*

that is, the *k*th Slepian function (i.e., the Fourier transform of the sequence denoted by $\nu_k(t)$) is

$$\hat{y}_k = x_k(f) - \hat{\mu}_j \nu_k(f - \hat{f}_j) \qquad (51)$$

over a bandwidth $|f - \hat{f}_j| \lesssim 3W$ around each line. Recomputing the Loève spectrum and spectral coherences with $\hat{y}_k$, we obtain the result plotted in Fig. 6. The two "strong" peaks remaining in the figure are in the outer coherence part of the pilot and on the steep skirts of the VSB modulated signal. Conditions on the steep slopes represent a partial violation of the assumptions behind multitaper estimates: the spectrum is not "locally white." In such cases, the bias is still bounded in the usual way, but quadratic bias terms become more important. The biggest effect, however, is that the steep slope induces correlation between the different eigencoefficients, so the effective DoFs of the estimate are reduced. This is usually more of a problem when assessing significances of coherences and *F*-tests than it is for spectrum estimates, because significance levels of spectra are usually assessed at peaks than they are on slopes. The quadratic-inverse theory [60] was developed to extend multitaper estimates to situations where the assumption of "locally white" is unreasonable,
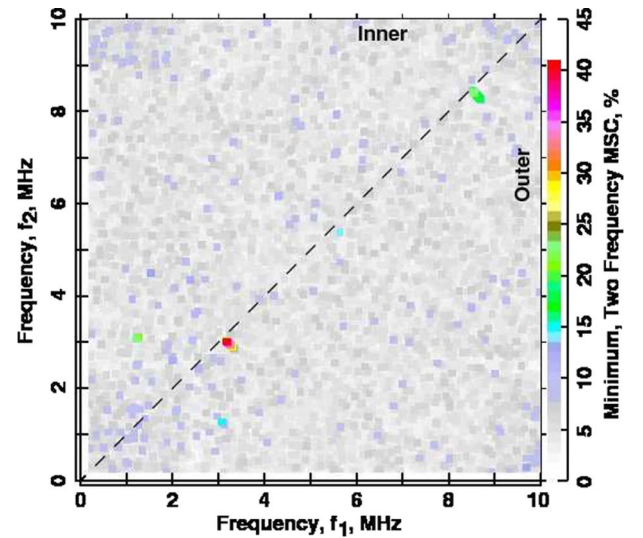
the data sequence is stationary. However, when the average power is varying, as in cognitive-radio applications, the estimated coherence will be dominated by the eigencoefficients with the highest power. Depending on changes in power, the effective degrees of freedom may only represent a single block. For a stationary process, the changes in block-to-block power are usually small. We are, however, not dealing with stochastic systems involving a stationary process but with wireless communications systems, and such systems commonly use dynamic power control where changes of 5 and 10 dB are common, as are transitions from "on" to "off."

Returning to the discussion of the peaks in Fig. 4, we note that many of these peaks are *not* evidence for cyclostationarity but simply artifacts of the narrow-band components evident in Fig. 3. The problem, simply put, is that one sinusoid looks much like another; and, if we have clean sinusoidal components, then they will appear coherent with each other.

Fig. 5 shows a harmonic *F*-test for one of the data segments in the ASTC-DTV example (the others are similar). In this figure, five lines are identified as significant above the 99.9% level. Details on *harmonic F*-tests are given in [8] and [19]; the performance of these tests approaches the Cramér–Rao bound for frequency estimation. Denoting the frequencies estimated by the point where the *F*-test is maximized and above some specified threshold by $\hat{f}_j$ and the corresponding line amplitudes by $\hat{\mu}_j$, we may reshape the eigencoefficients by subtracting the effect of the lines;

Fig. 6. *A better estimate of the two-frequency coherence for the ATSC-DTV signal. The dataset is the same as in Fig. 4 but here periodic terms where the harmonic F-test exceeds the 99.9% significance level were subtracted from the eigencoefficients before computing $|C(f_1, f_2)|^2$. In contrast to the "raw" estimate of Fig. 4, there are no inner coherences above about ∼0.15, a value that could be just sampling fluctuations. The scales are different in Figs. 4 and 6. Note also that there are three strong peaks in the outer coherence near $(f_1, f_2) \sim (3, 1.2), (3.2, 2.9),$ and $(8.7, 8.3)$ MHz. The pixels corresponding to significant coherences have been enlarged. The differences between the frequencies in each pair correspond to the frequency offset $(f_2 - f_2) = \alpha$.*

that is, to estimate spectra *within* the inner bandwidth of the signal. Without going into detail, it was shown in [32] that the effective DoFs of a multitaper estimate are reduced by a steep slope in the spectrum by a term depending on the squared partial derivative $((\partial/\partial f)\ln S(f))^2$, as shown by

$$\hat{\nu} = \frac{2K}{1 + D_1\left(\frac{\partial}{\partial f}\ln S(f)\right)^2} \qquad (52)$$

where ln denotes the natural logarithm and

$$D_1 \approx \frac{4}{15}\frac{\sqrt{6}}{\pi}\cdot\frac{2NW}{K}\cdot W^2. \qquad (53)$$

The slope on the skirts of the ATSC-DTV signal is specified to be steep, so that the DoFs are reduced, which is the likely cause of the apparent coherences on the band edges in Fig. 6.

Looking at the IEEE P1631 specification for the ATSC-DTV, the transmitted power spectrum should drop by at least 11.5 dB/MHz near the channel edges and much more rapidly in the skirt region. With $K = 8$ tapers, using 11.5 dB/MHz for the derivative in (53) only costs about
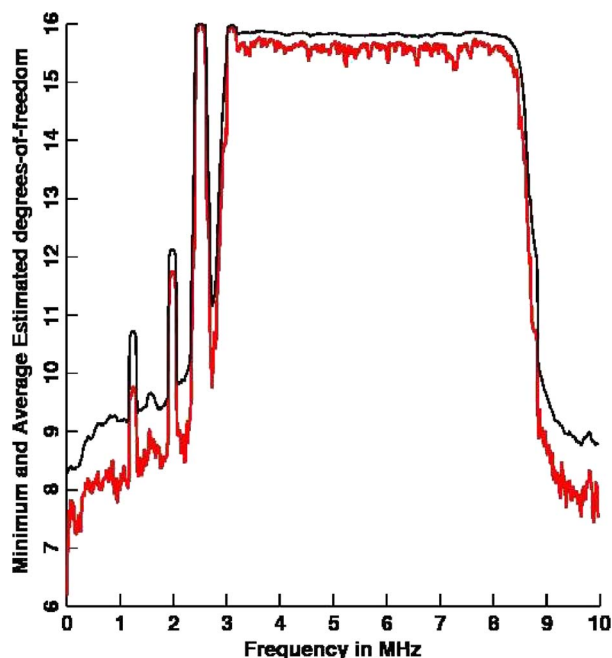

Fig. 8. *Bartlett's M-test for stationarity applied to the 50 MTM estimates for the $N = 1000$, $NW = 4.5$, and $K = 8$ estimates used in Fig. 7. This calculation is the usual one for M, except that the average DOF shown in Fig. 7 is used instead of the nominal value. It may be seen that the estimate is close to its expected value in the noise parts of the spectrum, slightly low in the main TV band, high near the band edges and both edges of the 2.518 MHz frequency-modulated carrier, and "superstationary" (excessive low) on the other carriers.*

Fig. 7. *Average and minimum estimated degrees of freedom for 50 estimates of the ATSC-DTV signal with $N = 1000$, $NW = 4.5$, and $K = 8$ windows. The reduced DoF on the lower parts of the spectrum (exactly the regions of interest for cognitive radio) is a main reason for recommending $NW = 8$.*
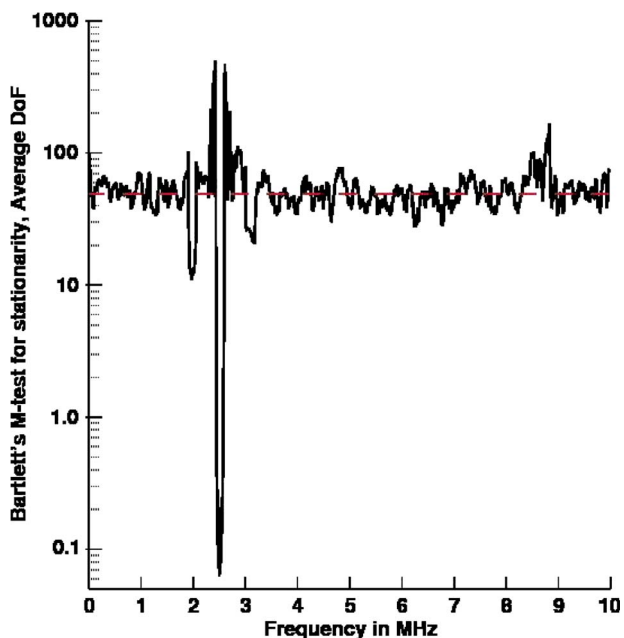
0.2 DoF. In the skirt region, however, the spectrum is close to being discontinuous, with the result that the partial derivative $(\partial/\partial f)\ln S(f)$ is unbounded. Numerically differentiating the logarithm of the average spectrum and using it in (54) predicts $\hat{\nu}$ to be approximately 1.05, implying that on these steep slopes, the spectrum obtained using $N = 1000$ is too steep to estimate reliably.

With the DoF's being variable, evaluating (12) for the ATSC-DTV example with $C_o = 4.5$ and $K = 8$ tapers gives the statistics summarized in Fig. 7. With this choice of parameters, approximately one-half of the degrees of freedom are lost near the band-edges. If we repeat the experiment with $C_o = 8$ and $K = 8$ on the same data, the minimum degrees of freedom are approximately 15.97; so, in this example, there is no need for adaptive weighting.

Fig. 8, involving the application of Bartlett's *M*-test, shows that stationarity is a reasonable assumption for the ATSC-DTV example with some exceptions. The figure shows less variability than expected on carriers; it is clearly nonstationary on band-edges and around what appears to be a frequency modulated carrier near 2.5 MHz. Also, the test is on the low side across most of the ATSC-DTV signal, showing that it is less variable than stationary Gaussian noise.

The overall message to take from the experimental results plotted in Figs. 3–8 on the ATSC-DTV signal is summarized as follows.

1) *Interfering signals do exist* in the ATSC-DTV, regardless of whether the TV station is switched on or off, as clearly illustrated in Fig. 3 for the "on" condition.

2) Although it is well recognized that the ATSC-DTV band is open for cognitive-radio applications when the pertinent TV station is switched off, the results presented in Fig. 3 are intended to demonstrate the high spectral resolution that is afforded by using the MTM for spectrum sensing. Obviously, an immediate benefit of such high spectral resolution is improved radio-spectrum underutilization, which, after all, is the driving force behind the use of cognitive radio.

3) The current FCC ruling on the use of white spaces in the ATSC-DTV band for cognitive-radio applications permits such use by low-power cognitive radios only when the TV station is actually switched off. Nevertheless, the results displayed in Fig. 3 clearly show the feasibility of using low-power cognitive radios in white spaces that exist below the pilot, and doing so without interference to the TV station when it is actually on, thereby resulting in additional improvement in radio-spectrum utilization.

4) In using the two-frequency magnitude-squared coherence $|C(f_1, f_2)|^2$ for the identification of cyclostationarity in the ATSC-DTV signal for example, care has to be taken.

B. Choice of Estimate and Computational Issues

Cognitive-radio applications require *reliable* spectrum estimates. The term "reliable" can be interpreted in many ways, but, in this paper, we mean that the estimate should have a *low and quantifiable bias plus low variance*. Simultaneously, it should make *efficient* use of the available data; there is little point in attempting to estimate a spectrum to check what bands are available if it requires such a large sample size that the spectrum changes significantly while the data are being acquired. A related requirement is that the computations be done *rapidly*. Lastly, "reliable" can also be interpreted as "robust," in the sense that the estimate should not depend on whether the data have a Gaussian, Laplacian, or any other possible distribution; it should not matter if the data are "random" or contain deterministic components; and the estimate is relatively tolerant of outliers.

Continuing the discussion on computational issues, multitaper estimators require relatively low computational resources. Assuming that the Slepian tapers (windows) are precomputed for a prescribed size K, each eigencoefficient in the MTM can be computed with a FFT of the data times the sequence. With routines such as FFTW, which, according to

[61], stands for "Fastest Fourier transform in the West," the computation is fast to begin with and we can do "tricks" to speed up the process even further. If we have real-valued data, then we can obviously do two eigencoefficients with each FFT. Similarly, we can split the data into even and odd parts of length $N/2$, the tapers are alternatively even and odd, and we can split the Fourier transform into odd and even parts, then ignore all the calculations that result in zero; the resulting code is messy but fast. Finally, if we take $NW = 8$, the bandwidth of the estimates involves eight Rayleigh resolutions $N/(2W)$, so we need only compute every eighth FFT bin to get a reasonable approximation of the spectrum. Using the speeds given for FFTW3[10] for a single precision 3 GHz Intel Xeon Core Duo, a single precision 1024-point complex transform requires about 3.8 μs. Assuming the use of real data and computing two sets of eigencoefficients with each FFT, the $K = 8$ spectrum estimate would require about 15 μs.

The message to take from the remarks presented herein is thus summarized as follows:

> By precomputing the Slepian tapers and using the state-of-the-art FFT algorithm, computation of the MTM for spectrum sensing can be accomplished in a matter of 5 to 20 μs, which is relatively fast for cognitive-radio applications.

C. Loève Coherences

Estimation of the Loève magnitude-squared coherence, using the TF-MSC formulas of (33) and (34), is relatively slow. This estimation uses the same eigencoefficients but does the coherence estimates (in the ATSC-DTV example) on one-half of a 512 × 512 grid; it could therefore take about 600 μs.

If we have L frequencies, then the eigencoefficients may be thought of as an L-by-K matrix, denoted by $\mathbf{Y}$. Thus, the Loève spectrum is proportional to the outer product $\mathbf{YY}^\dagger$, where, as noted previously, $\dagger$ denotes Hermitian transposition, and the coherences are the same, with each row of the matrix $\mathbf{Y}$ standardized to have unit length. These product matrices are, at most, rank K, and this information is contained in the SVD of $\mathbf{Y}$. For typical values of L and K, dealing with an L-by-K SVD is clearly much faster than its M-by-M outer product; the exact improvement in computing the estimate of TF-MSC is application-dependent.

D. Fourier Coherences

Fig. 4 illustrates one way of viewing cyclostationarity characterization of the ATSC-DTV signal using the inner spectral coherence of (33) and outer spectral coherence of (34), rooted in the MTM-Loève theory. Fig. 9 completes the experimental study of the ATSC-DTV signal, viewed from the Fourier-theory perspective.
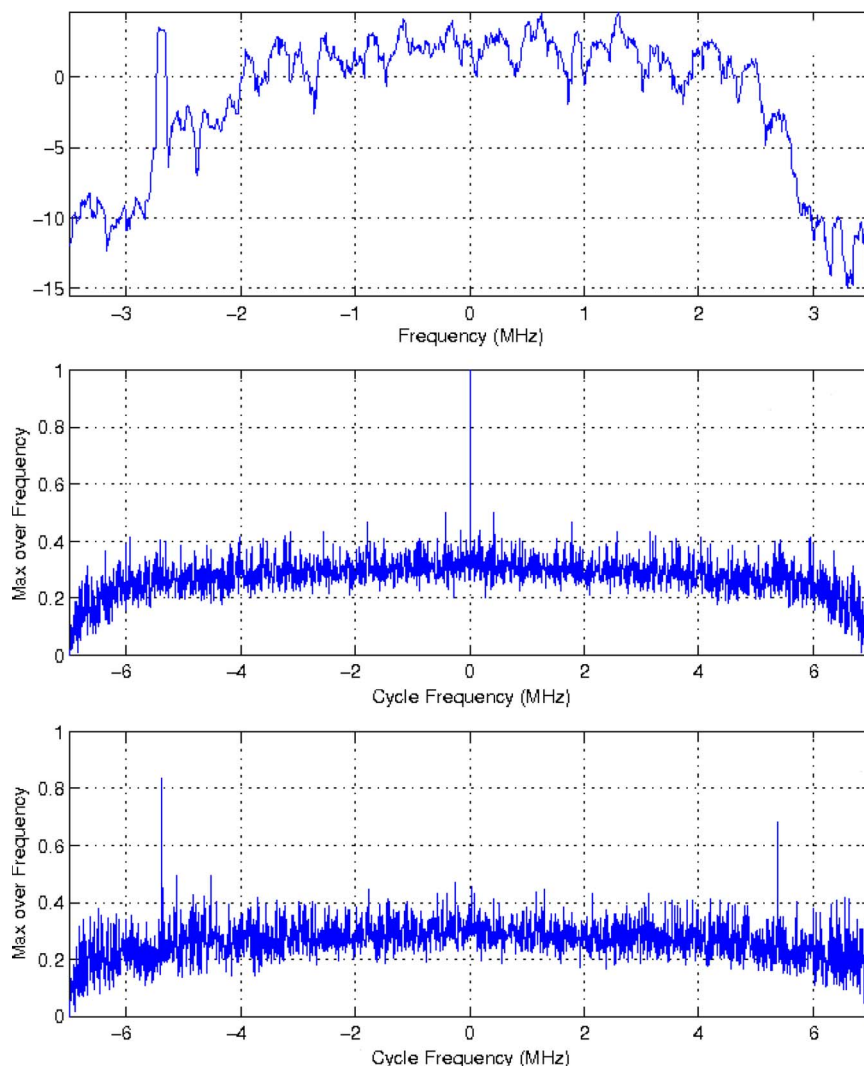
---

[10]See www.fftw.org.

Fig. 9. *(a) Windowed periodogram of 160 μs of ATSC-DTV data. (b) Inner spectral coherence of the ATSC-DTV data, computed using (44). (c) Outer spectral coherence of the ATSC-DTV signal, computed using (45). (Reproduced with the permission of Dr. C. Spooner.)*

Fig. 9, consisting of three parts, was obtained using 160 μs of ATSC-DTV data. From the power spectrum of the ATSC-DTV signal plotted in Fig. 3, we know the location of the pilot to be at 2.69 MHz below the center frequency of the ATSC-DTV signal. This point is borne out by the windowed periodogram plotted in Fig. 9(a).

Fig. 9(b) and (c) plot the maximum over frequency versus the cycle frequency α, which is defined as the difference frequency between $(f + \alpha/2)$ and $(f - \alpha/2)$ for a fixed carrier f. Except for the trivial result pertaining to frequency parameter $\alpha = 0$, Fig. 9(b) based on the spectral coherence formula of (44) exhibits no significant inner cyclostationarity of the ATSC-DTV signal. In direct contrast, Fig. 9(c) based on the outer spectral coherence given of (45) exhibits two strong features at ± 5.39 MHz. For analytic justification of these two features, let f_{pilot} and f_{symbol} denote the pilot frequency 2.69 MHz and the

symbol rate 10.76 Msymbols/s. Analysis of the heavily asymmetrically filtered eight-level pulse-amplitude modulated (8-VSB) signal confirms the results of Fig. 9(c):

- one feature at $2 \times f_{\text{pilot}} = -5.38$ MHz;
- a second feature at $2 \times f_{\text{pilot}} + f_{\text{symbol}} = -5.38 + 10.76 = +5.38$ MHz.

A direct comparison of Figs. 4 and 9 is somewhat difficult for the following reasons.

1) The major difference is in the manner in which the data were collected. Fig. 4 is based on real-valued ATSC-DTC data sampled at 20 MHz rate with the origin 5 MHz below the carrier. This gives a frequency range of ± 5 MHz around the carrier. Because the main spectral coherence features in the ATSC-DTV are expected to be ± 5.38 MHz from the carrier, this is a serious limitation. It is possible that the series of peaks

just above the f_2 axis in Fig. 4 are aliases. The data in Fig. 9, in contrast, use complex-valued data centered on the carrier with a 7 MHz sampling rate. This is clearly adequate to show the ±5.38 MHz outer coherences. The frequency range was truncated for aesthetic purposes. However, having f_0 fixed at the carrier frequency, the numerous other peaks visible in Fig. 4 are missed.

2) Fig. 4 is a composite of two symmetric figures with inner coherences above the diagonal and outer coherence below.

3) The diagonal element corresponding to the strong line at the origin of Fig. 9(b) is suppressed in Fig. 4.

4) Frequencies are plotted relative to the sampling origin in Fig. 4 and from the carrier frequency in Fig. 9.

5) Fig. 4 is given as a function of f_1 and f_2, and Figs. 9(b) and 9(c) as a function of the parameter α, where, as noted earlier, $f_1 = f_0 + \alpha/2$ and $f_2 = f_0 - \alpha/2$, here with f_0 set to the carrier frequency.

6) Fig. 4 is the *minimum* coherence at each (f_1, f_2) pair taken over 20 disjoint segments. Also, the regions around high peaks have been broadened artificially to make them more visible. There are *many* frequency pairs in both the inner and outer regions where the minimum is between 0.1 and 0.15. With 20 segments and eight Slepian tapers per segment, the probability of the minimum TF-MSC's exceeding 0.1 in uncorrelated data is $= (1 - 0.1)^{140} 40 \times 10^{-7}$, implying there is considerable structure in addition to the main peaks seen in Fig. 9. This is in reasonable agreement with the coherences seen in the lower two panels of Fig. 9. In these, the squared coherences are generally between 0.2 and 0.4, so a minimum of 0.1 to 0.15 in 20 segments is very reasonable.

The comparison of Figs. 4 and 9 would be incomplete without bearing in mind the following point: Fig. 9 assumes the availability of the carrier, which is obtained from part (a) of the figure. On the other hand, no such assumption is made in Fig. 4, and, for that matter, Figs. 6 and 12. If this assumption was made in computing the Loève spectral coherences of (33) and (34), then computations of Figs. 4, 6, and 12 would be considerably simplified.

VIII. SECOND EXAMPLE: GENERIC LAND-MOBILE RADIO SIGNAL

In Section II, we pointed out that spectrum holes may also be found in commercial cellular bands. Therefore, for the second application of the MTM, we consider a generic land-mobile radio (LMR), using QPSK for modulating the data. The signal used in the study was recorded as a complex data stream at a fixed suburban location using a 96 kHz sampling rate, with the mobile unit traveling at a speed of 65 km/h with carrier frequency of 1.9 GHz.

To begin, Fig. 10 shows a multitaper dynamic spectrum over 50 ms. The data blocks are 500 samples (2.6 ms) long and offset by 120 samples, or 0.62 ms. Here we used a time–bandwidth product $C_o = 8$, with $K = 8$ and adaptive weighting. Fig. 11 shows the minimum, arithmetic mean, geometric mean, and maximum spectra over the 77 sections, making up the dynamic spectrum shown in Fig. 10. Looking at Figs. 10 and 11, the main signal (centered on the carrier) is clearly seen, as are a second fading signal 50–60 dB down and approximately 45 kHz higher in frequency, plus a nonfading carrier 80 kHz below the main signal. We also note that the difference between the arithmetic and geometric means is larger on the fading signals than it is in the noise parts of the spectrum. This is to be expected because the log-ratio of the two means is, except for a scale factor, Bartlett's M-test for homogeneity or, when applied to a spectrogram as it is here, a test for stationarity. In Section IX, implications of the fading phenomenon are examined.

As an incidental point, Fig. 12 shows a plot of the two-frequency inner coherence between two antennas spaced a wavelength apart for the LMR data. Here, the existence of cyclostationarity is clearly illustrated in the figure.
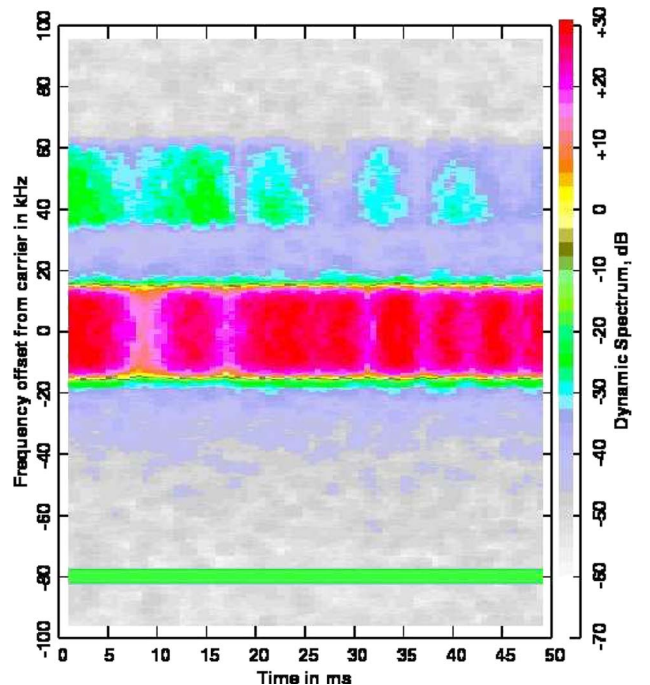

Fig. 10. *A multitaper spectrogram (or dynamic spectrum) using 2.6 ms (500 samples) data blocks. The data blocks were offset by 0.62 ms (120 samples) and the estimates computed with a time–bandwidth $C_o = 8$ and $K = 8$ windows with adaptive weighting. The carrier is at ~1.9 GHz, and we can see both a strong fading channel around the carrier, which is probably a second-ring fading signal two channels above and about 60 dB down from the main signal, and an unmodulated, steady carrier about 80 kHz below the main signal. In this example, the mobile unit was travelling at ~60 km/h.*
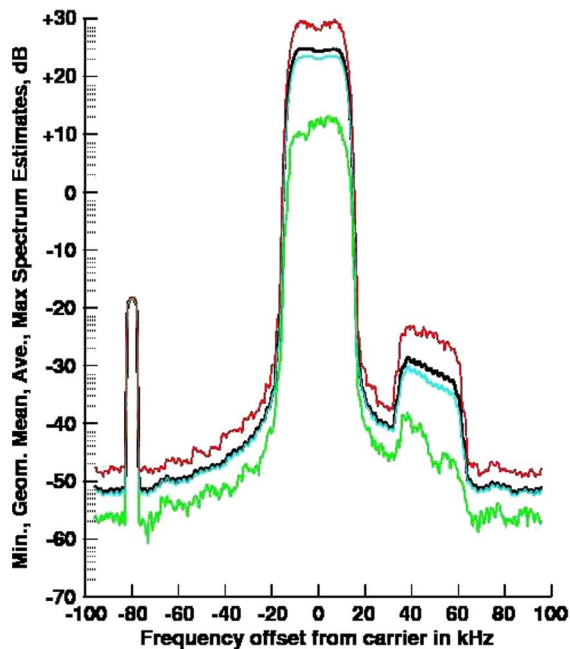
Fig. 11. *Minimum, geometric mean, arithmetic mean, and maximum spectrum estimates obtained from 77 2.6 ms (500 samples) data blocks. The log-ratio of the arithmetic and geometric means is, within a scale factor, Bartlett's M-test; see footnote 7. It can be seen that the parts of the signal that are mostly noise, that is, with level $S \sim 10^{-5}$, are reasonably stationary, whereas in both active channels, there is a noticeable gap between them. At the unmodulated carrier at ~ -80 kHz, in contrast, all four curves overlap.*

The choice of $C_o = 8$ may seem large, but communication systems have large dynamic ranges. We may commonly have to deal with spectra where the dynamic range is over 100 dB. The choice of $C_o = 8$ with $K = 8$ tapers gives a dynamic range better than 90 dB *without* adaptive weighting, as illustrated in Fig. 13, where the four lowest order tapers have a range of at least 150 dB. However, in many applications, accuracy will be limited by ordinary floating-point arithmetic and the resolution of analog-to-digital conversion, and not by intrinsic properties of the windows.

The next problem to be dealt with is that of choosing the block size N or, in physical units, $N\Delta t$, where Δt is the sampling interval. For a given choice of C_o, the bandwidth on each side of a given frequency is $W = C_o/N$ or $B = C_o/(N\Delta t)$ Hz, so the total bandwidth is $2B$. In these applications, we recommend the use of C_o greater than four, with $C_o = 6$ or $C_o = 8$ being a reasonable value. The choice of N, however, depends on the complexity and assigned channel allocations in the band being used.

Fig. 14 shows spectra estimated from the first N samples of the LMR data with N being 50, 100, 250, and 1000, all with $C_o = 8$. (The case of $N = 500$ was shown previously in Fig. 11.) Clearly, the $N = 50$ spectrum does not really resolve the two fading signals, and it spreads the
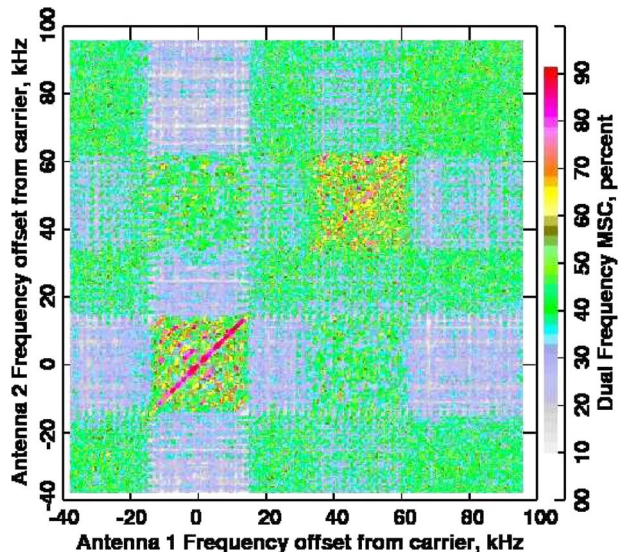

Fig. 12. *Inner two-frequency MSC between two antennas for the LMR signal, excluding the region with the carrier. Cyclostationarity in the stronger signal is obvious, and moderately so in the weaker one.*
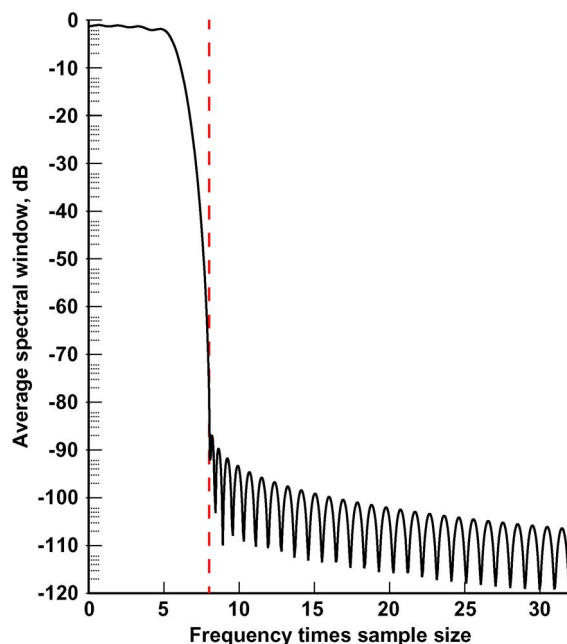

Fig. 13. *The average spectral window of a multitaper estimate with $C_o = 8$ and $K = 8$ tapers. The first sidelobe, just above the red dashed vertical line that marks the bandwidth W in Rayleigh resolution units, is more than 90 dB down and drops to over 100 dB by approximately 15 Rayleigh resolution units. If this calculation is repeated with just the first $K = 4$ windows, using 32-bit floating-point, we hit roundoff noise around 150 dB down.*

80 kHz carrier over approximately 40 kHz. The $N = 100$ spectrum is clearly better, and either could be used if the choice was for fast computation. We note that we could
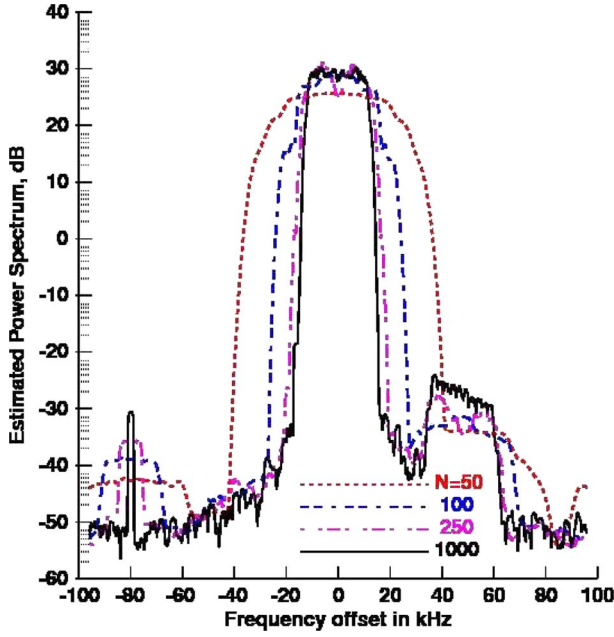
Fig. 14. *Spectra for sample sizes N = 50, 100, 250, and 1000, beginning at the start of the data whose dynamic spectrum is shown in Fig. 10. In all cases, we have used a single data section, a time–bandwidth $C_o = 8$, $K = 8$ windows, and adaptive weighting.*

alternatively use long blocks to estimate where the channels are, then use short blocks to estimate when one of the channels becomes available. In this example, the choice $N = 250$ is close to the performance of the $N = 1000$ estimate and, without an explicit optimality criterion, it might be a good choice. The adaptive weights converged in a maximum of three iterations, producing estimates with *minimum* degrees of freedom of approximately 15.5 and clearly showing the main features in the spectrum. So, other things being equal, the $N = 250$ estimate is a reasonable choice. At the 96 kHz sampling rate, $N = 250$ corresponds to a 2.6 ms block, and the choice $N = 100$ would give a reasonable performance with approximately 1 ms blocks. There is, however, still the problem of fading to be considered, which is done in the next section.

IX. RAYLEIGH FADING CHANNELS

Because mobile communications are one of the probable applications of cognitive radio, we must consider the spectrum-estimation problem in a *Rayleigh fading channel*. To proceed, consider a data-transmission system for a Rayleigh-fading channel where $X(t)$ denotes the transmitted signal and $C(t)$ is a complex narrow-band Gaussian process defining the instantaneous channel characteristics. The received signal is defined by

$$Y(t) = C(t) \cdot X(t) + N(t) \qquad (54)$$

where $N(t)$ is stationary, complex, white Gaussian noise. Here we assume a *Jakes model* [62] for the channel, that is, the autocorrelation function of $C(t)$ is

$$R(\tau) = \mathbf{E}\{C(t)C^*(t+\tau)\} = J_0(2\pi f_d \tau) \qquad (55)$$

where, as before, $\mathbf{E}$ is the statistical expectation operator, the mean-square transfer through the channel is normalized to unity, $J_0(\cdot)$ is the Bessel function of zero order, f_d is the Doppler frequency, and τ is the time delay. The Doppler frequency is $f_d = (v/c)f_c$, where v is the mobile velocity, f_c is the carrier frequency, and c is, as usual, the velocity of light. Denoting the wavelength by $\lambda = c/f_c$ and distance by $s = v\tau$, the argument of the Bessel function J_0 is just $2\pi(s/\lambda)$. Note that the covariance function $R(\tau)$ is simply a function of the distance moved during time τ measured in wavelengths.

There are at least two problems with the Jakes model. First, it assumes that the received signal is a result of signals reflected from a two-dimensional array of *random* scatterers; a glance at many buildings, with their rows of uniformly-spaced windows or wall panels, suggests that a diffraction grating might be a better model. Secondly, the Bessel function $J_0(\cdot)$ is a *bandlimited* function and implies that the fading process is deterministic. It is, in fact, just the leading term of a series; see [63]. Nevertheless, it is adequate to explain many of the commonly encountered fading problems in practice. The explanation for the ripples is relatively simple. Consider the model of (54) as part of a spectrum-estimation problem and write the eigen-coefficients as follows, ignoring the additive noise in (54):

$$y_k(f) = \sum_{t=0}^{N-1} C(t)x(t)v_t^{(k)} \exp(-j2\pi ft). \qquad (56)$$

Now, consider the data taper to be the product $C_k(t) = C(t)v_t^{(k)}$; so the estimated eigenspectra $\hat{S}_{C,k}(f)|y_k(f)|^2$ will be the true spectrum convolved with an equivalent spectral window. The Fourier transform of $J_0(2\pi f_d \tau)$ is defined on the infinite interval $(-\infty, \infty)$ by

$$\tilde{C}(f) = \begin{cases} \frac{1}{\pi}\left[f_d^2 - f^2\right]^{-\frac{1}{2}}, & \text{for } |f| < |f_d| \\ 0, & \text{otherwise.} \end{cases} \qquad (57)$$

Equation (57) implies that the expected value of the spectrum will be that from nonfading conditions $S_{nf}(f)$ convolved with $\tilde{C}(f)$. This convolution poses a problem because $\tilde{C}(f)$ goes to infinity at $f \pm f_d$, and the power in the sidelobes of the windows decays asymptotically as f^{-2}, which is a characteristic of QPSK signaling; hence, formal convergence is problematic. In particular, the sidelobes of the Slepian sequences are asymptotically of the form

$c_k \text{sinc}(fT)$, where $\text{sinc}(\cdot)$ denotes the sinc function. So, when adjacent sidelobes are spaced by $2f_d$, that is, when $T \approx 1/(2f_d)$, we should expect the presence of large ripples in the spectrum. On shorter time intervals, the tendency for the Fourier transform to have a maximum at the Doppler frequency is still present. In this example, the Doppler frequency is approximately 112 Hz. Consequently, when the resolution of the spectral estimator becomes finer than this value, we begin to see ripples. We emphasize that these ripples are *not* sidelobes of the spectral windows per se because, as seen in Fig. 15, these windows can resolve the spectrum without adaptive weighting. The procedure, however, is sensitive, and as the spacing of the Doppler sidelobes begins to match those of the windows, we can change the effective sidelobe level by about a factor of three, which causes the adaptive weights to oscillate. Heuristically, looking at Fig. 11 and recalling that at a 96 kHz sampling rate, a sequence of 2000 samples is about 20 ms, the data windows include three high-energy portions of the signal. Consequently, we should not use excessively long data blocks in a fading environment. A more effective approach is to use several moderate lengths; (for example, we may choose $N = 250$ or $N = 500$) followed by robust estimation at each frequency.

X. SUMMARY AND DISCUSSION

In finding and then exploiting spectrum holes in ATSC-DTV and commercial cellular bands, cognitive radio has the potential to solve the radio-spectrum underutilization
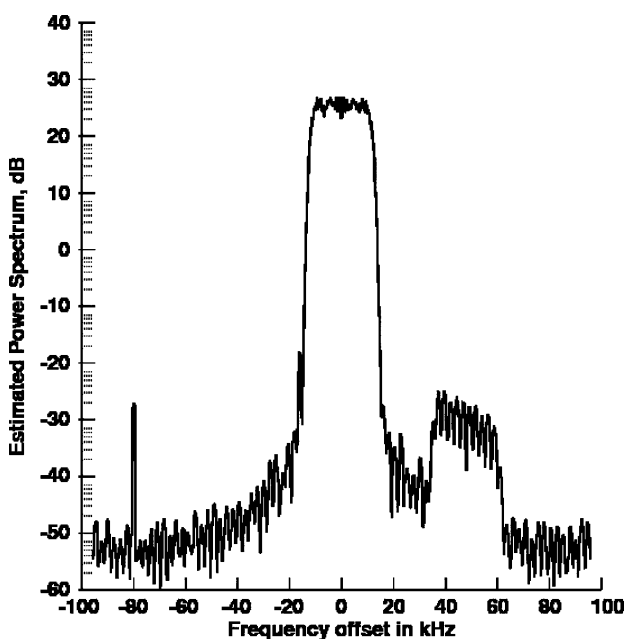

Fig. 15. *An estimate of the spectrum using the same LMR data set and parameters used in Fig. 14, but here with N = 2000. Note the prominent "ripples" in the lower parts of the spectrum.*

problem. However, when the following compelling practical issues are recognized, we begin to appreciate the research and development challenges involved in building and commercializing cognitive radio:

- the notoriously unreliable nature of wireless channels due to complexity of the underlying physics of radio propagation [10], [64];
- the uncertainties surrounding the availability of spectrum holes as they come and go [65];
- the need for reliable communication whenever and wherever it is needed [2], [3].

A. The Multitaper Method: A Tool for Integrated Nonparametric Spectrum-Sensing of the RF Environment

In signal-processing terms, spectrum-sensing of the radio environment in an unsupervised manner is one of those challenges on which the whole premise of cognitive radio rests. The MTM is a nonparametric (i.e., model-independent) and, therefore, *robust spectral estimator* that offers the following attributes for solving the radio-spectrum underutilization problem.

i) *Resolution of the bias-variance dilemma,* which is achieved through the use of Slepian sequences with a unique and remarkable property:

The Fourier transform of a Slepian sequence (window) has the maximal energy concentration inside a prescribed bandwidth under a finite sample-size constraint.

Simply put, there is no other window that satisfies this property.[10] Consequently, the MTM is an *accurate* spectral estimator, as evidenced by the experimental results on ATSC-DTV and generic land-mobile radio signals, presented in Sections VII and VIII, respectively.

ii) *Real-time computational feasibility,* which is realized through prior calculation and storage of the desired Slepian coefficients for a prescribed time–bandwidth product and use of a state-of-the-art FFT algorithm.

iii) *Multidirectional listening capability,* which is achieved by incorporating the MTM into a *space–time processor* for estimating the unknown directions of arrival of interfering signals.

iv) *Cyclostationarity,* the characterization of which is performed by expanding the MTM to embrace the

---

[10]Of the various windows described in the literature, the Kaiser window [66], gives a good approximation to the zeroth-order prolate spheroidal wave function, that is, the Slepian taper $\{v_t^{(0)}\}_{t=1}^N$. This window is based on an analytic approximation due to Rice [67] and, unlike fixed-parameter windows such as the Hamming and Parzen windows (that correspond roughly to time–bandwidth products of $NW = 2$ and $NW = 4$, respectively), has an adjustable parameter α, which maps to the time-bandwidth product $C_o = NW$ defined in Section III. However, there does not appear to be a simple equivalent of the Slepian sequence with $k \geq 1$.

Loève transform that accounts for nonstationarity of incoming RF stimuli in a mathematically rigorous manner; the property of cyclostationarity provides an effective approach for the reinforced detection of spectrum holes and the classification of communication signals.

The message to take from the combination of these four attributes is summed up as follows. The multitaper method is a method of choice for nonparametric spectrum-sensor that is capable of detecting spectrum holes in the radio band, estimating the average power in each subband of the spectrum, providing a sense of direction for estimating the wavenumber spectrum of interferers, and outputting cyclostationarity characterization of the receiver input for signal detection and classification; just as importantly, computation of this overall spectrum-sensing capability is feasible in real time.

B. Loève and Fourier Theories of Cyclostationarity

Cyclostationarity is an inherent property of digital modulated signals that exhibit *periodicity*. It manifests itself in time–frequency analysis of such signals.

The Loève theory of TFA paves the way for finding cyclostationarity in a signal through the combined use of two complementary spectral parameters, namely, the inner and outer spectral coherences. The spectral coherence is said to be of the inner kind when the spectral correlation in its numerator is defined as the expectation $\mathbf{E}[X_k(f_1)X_k^*(f_2)]$, in which the $X_k(f)$ is the multitaper Fourier transform of the input signal $x(t)$ at frequency f. It is said to be of the outer kind when its numerator is defined as the expectation $\mathbf{E}[X_k(f_1)X_k(f_2)]$, which does not involve complex conjugation.

The Fourier theory of cyclostationarity exploits the periodic property of the autocorrelation function of a cyclostationary process, or its power spectrum. In its own way, the Fourier theory also leads to the formulation of spectral coherences of the inner and outer kinds, which are defined in a manner similar to their Loève counterparts.

The Loève and Fourier theories of cyclostationarity are indeed related in signal-processing terms, as discussed in Section VI. Perhaps the way to distinguish between them is to say that when a nonstationary processes is considered, the Loève theory applies to any such process, whereas the Fourier theory is restricted to a cyclostationary process.

C. The Fading Phenomenon

The notoriously unreliable nature of wireless channels is attributed to the fading phenomenon in electromagnetic radio propagation. This important issue was addressed in Section IX by focusing on *Rayleigh fading channels,* based on *Jake's model.* Although this model is incomplete in theoretical terms, it is adequate to explain many of the fading problems commonly encountered in practice. An important point to take from the discussion presented in Section IX is that in a fading environment, the use of excessively long data blocks should be avoided.

D. Filter-Bank Implementation of the MTM

Last, but by no means least, Farhang-Boroujeny [68] has shown that the underlying analytic theory of the MTM, leading to the derivation of the multitaper spectral estimator, can indeed be reformulated in the framework of filter banks. In effect, the orthogonal sequence of Slepian sequences (windows) is viewed as an *orthogonal bank of eigenfilters;* hence the new terminology "filter-bank spectral estimator." Implementation of the filter bank involves the use of a prototype low-pass filter that realizes the zeroth band of the filter bank. The remaining bands in the filter bank are realized through the use of *polyphase modulation.*

What is pleasing about the filter-bank approach of deriving the multitaper spectral estimator is not only its novelty but also the fact that the theory of filter banks is well known in signal-processing literature [69]. ∎

REFERENCES

[1] FCC, "Spectrum policy task force," Tech. Rep., Nov. 2002.

[2] S. Haykin, "Cognitive radio: Brain-empowered wireless communications," *IEEE J. Sel. Areas Commun.*, vol. 23, pp. 201–220, Feb. 2005.

[3] S. Haykin, "Fundamental issues in cognitive radio," in *Cognitive Wireless Communication Networks*, E. Hossain and V. K. Bhargava, Eds. New York: Springer, 2007, pp. 1–43.

[4] R. Tandra, S. M. Mishra, and A. Sahai, "What is a spectrum hole and what does it take to recognize one?" *Proc. IEEE*, vol. 97, Mar. 2009.

[5] S. Shellhammer, S. Shankar, R. Tandra, and J. Tomcik, "Performance of power detector sensors of dtv signals in ieee 802.22 WRANs," in *Proc. 1st ACM Int. Workshop Technol. Policy Access. Spectrum (TAPAS)*, Aug. 2006. [Online]. Available: http://doi.acm.org/10.1145/123488.1234392

[6] H. Chen and W. Gao, "Text on cyclostationary feature detector—Information annex on sensing techniques," in *IEEE 802.22 Meeting Doc.*, Jul. 2007. [Online]. Available: https://mentor.ieee.org/802.22/file/07/22-07-0283-00-000-text-on-cyclostationary-feature-detector-thomson.doc

[7] R. Tandra and A. Sahai, "SNR walls for signal detection," *IEEE J. Sel. Topics Signal Process.*, vol. 2, pp. 4–17, Feb. 2008.

[8] D. J. Thomson, "Spectrum estimation and harmonic analysis," *Proc. IEEE*, vol. 70, pp. 1055–1096, Sep. 1982.

[9] E. Serpedin, F. Panduru, I. Sari, and G. B. Giannakis, "Bibliography on cyclostationarity," *Signal Process.*, vol. 85, no. 12, pp. 2233–2303, 2005.

[10] J. Parsons, *The Mobile Radio Propagation Channel.* New York: Wiley, 2000.

[11] FCC, "Report and order on TV white space," Nov. 2008. [Online]. Available: http://hraunfoss.fcc.gov/edocs_public/attachmatch/FCC-08-260A1.pdf

[12] M. M. Buddhiko, "Understanding dynamic spectrum access: Models, taxonomy and challenges," in *Proc. IEEE DySPAN 2007*, Apr. 2007.

[13] A. P. Subramanian, H. Gupta, S. R. Das, and M. M. Buddhiko, "Fast spectrum allocation in coordinated dynamic spectrum access based cellular networks," in *Proc.IEEE DySPAN 2007*, Apr. 2007.

[14] J. P. Burg, "Maximum entropy spectral analysis," Ph.D. dissertation, Stanford Univ., 1975.

[15] D. Slepian, "Prolate spheroidal wave functions, fourier analysis, and uncertainty v: The discrete case," *Bell Syst. Tech. J.*, vol. 57, pp. 1371–1429, Apr. 1989.

[16] D. Percival and A. Walden, *Spectral Analysis for Physical Applications*. Cambridge, U.K.: Cambridge Univ. Press, 1993.

[17] P. Welch, "The use of fast fourier transform for estimation of power spectra: A method based on time averaging over short, modified periodograms," *IEEE Trans. Audio Electroacoust.*, vol. AE-15, pp. 70–73, Jun. 1967.

[18] D. J. Thomson and A. D. Chave, "Jacknifed error estimates for spectra, coherences, and transfer functions," in *Advances in Spectrum Analysis and Array Processing*, vol. 1, S. Haykin, Ed. Englewood Cliffs, NJ: Prentice-Hall, 1991, pp. 58–113.

[19] A. Drosopoulos and S. Haykin, "Angle-of-arrival estimation in the presence of multipath," in *Adaptive Radar Signal Processing*, S. Haykin, Ed. New York: Wiley, 2007.

[20] A. Drosopoulos and S. Haykin, "Adaptive radar parameter estimation with Thomson multiple-window method," in *Adaptive Radar Detection and Estimation*, S. Haykin and A. Steinhardt, Eds. New York: Wiley, 1992, pp. 381–461.

[21] J. S. L. Marple, *Digital Specral Analysis With Applications*. Englewood Cliffs, NJ: Prentice-Hall, 1987.

[22] R. Schmidt, "A signal subspace approach to multiple emitter of location and spectral estimation," Ph.D. dissertation, Stanford Univ., Stanford, CA, 1981.

[23] R. Kumaresan and D. W. Tufts, "Estimating the angles of arrival of multiple plane waves," *IEEE Trans. Aerosp. Electron. Syst.*, vol. AES-19, pp. 134–139, Jan. 1983.

[24] T. P. Bronez, "On the performance advantage of multitaper spectral analysis," *IEEE Trans. Signal Process.*, vol. 40, pp. 2941–2946, 1992.

[25] S. Haykin, *Adaptive Filter Theory,* 4th ed. Englewood Cliffs, NJ: Prentice-Hall, 2002.

[26] D. J. Thomson, L. J. Lanzerotti, F. L. Vernon, III, M. R. Lessard, and L. T. P. Smith, "Solar modal structure of the engineering environment," *Proc. IEEE*, vol. 95, pp. 1085–1132, 2007.

[27] M. Loève, "Fonctions aléatoires de second ordre," *Rev. Sci.*, , pp. 195–206, 1946.

[28] M. Loève, *Probability Theory*. New York: Van Nostrand, 1963.

[29] S. Haykin and D. Thomson, "Signal detection in a nonstationary environment reformulated as an adaptive pattern classification problem," *Proc IEEE (Special Issue on Intelligent Signal Processing)*, vol. 86, pp. 2325–2344, Nov. 1998.

[30] L. Cohen, *Time-Frequency Analysis*. Englewood Cliffs, NJ: Prentice-Hall, 1995.

[31] L. Rayleigh, "On the spectrum of an irregular disturbance," *Philos. Mag.*, vol. 41, pp. 238–243, 1903.

[32] D. J. Thomson, "Multitaper analysis of nonstationary and nonlinear time series data," in *Nonlinear and Nonstationary Signal Processing*, W. Fitzgerald, R. Smith,

A. Walden, and P. Young, Eds. Cambridge, U.K.: Cambridge Univ. Press, 2001, pp. 317–394.

[33] C. Spooner, private communication, 2008.

[34] B. Picinbono, "Second-order complex random vectors and normal distributions," *IEEE Trans. Signal Process.*, vol. 44, pp. 2637–2640, 1996.

[35] C. N. K. Moores, "A technique for the cross-spectrum analysis of pairs of complex-valued time series, with emphasis on properties of polarized components and rotational invariants," *Deep-Sea Res.*, vol. 20, pp. 1129–1141, 1973.

[36] D. J. Thomson and S. Haykin, "Time-frequency analysis of sea clutter," in *Adaptive Radar Signal Processing*, S. Haykin, Ed. New York: Wiley, 2007, pp. 91–106.

[37] G. A. Prieto, F. L. Vernon, G. Masters, and D. J. Thomson, "Multitaper wigner-ville spectrum for detecting dispersive signals from earthquake records," in *Proc. 39th Asilomar Conf. Signals, Syst. Comput.*, 2005, pp. 938–941.

[38] W. A. Gardner and C. M. Spooner, "Signal interception: Performance advantages of cyclic feature detectors," *IEEE Trans. Commun.*, vol. 40, pp. 149–159, 1992.

[39] W. A. Gardner, "Spectral correlation of modulated signals, Part I analog modulation," *IEEE Trans. Commun.*, vol. COM-35, pp. 584–594, 1987.

[40] W. A. Gardner, W. A. Brown, and C. K. Chen, "Spectral correlation of modulated signals: Part II—Digital modulation," *Proc. IEEE*, vol. 35, no. 6, pp. 595–061, 1987.

[41] K. Kim, I. A. Akbar, K. K. Bae, J. S. Um, C. M. Spooner, and J. H. Reed, "Cyclostationary approaches to signal detection and classification in cognitive radio," in *Proc. IEEE DySPAN 2007*, Apr. 2007.

[42] C. K. Chen, "Spectral correlation characterization of modulated signals with application to signal detection and source location," Ph.D. dissertation, Dept. of Electrical Engineering and Computer Science, Univ. of California, Davis, 1989.

[43] W. A. Gardner, "Signal interception: A unifying theoretical framework for feature detection," *IEEE Trans. Comm.*, vol. 36, pp. 897–906, 1988.

[44] K. W. Kim, C. M. Spooner, I. Akbar, and J. H. Reed, "Specific emitter identification for cognitive radio with application to IEEE 802.11," in *Proc. IEEE GLOBECOM 2008*, 2008, pp. 1–5.

[45] W. A. Gardner and C. K. Chen, "Selective source location by exploitation of spectral coherence," in *Proc. 4th Annu. ASSP Workshop Spectrum Estimat. Model.*, Minneapolis, MN, 1988, pp. 271–276.

[46] J. H. Reed and T. C. Hsia, "The performance of time dependent adaptive fitters for interference rejection," *IEEE Trans. Acoust., Speech, Signal Process.*, vol. 38, pp. 1373–1385, 1990.

[47] B. C. Agee, S. V. Schell, and W. A. Gardner, "Spectral self coherence restoral: A new approach to blind adaptive signal extraction using antenna arrays," *Proc. IEEE*, vol. 78, pp. 753–767, 1990.

[48] G. B. Giannakis and E. Serpedine, "Blind identification of ARMA channels with periodically modulated inputs," *IEEE Trans. Signal Process.*, vol. 46, pp. 3099–3104, 1998.

[49] H. L. Hurd and A. Miamee, *Periodically Correlated Random Sequences*. New York: Wiley, 2007.

[50] W. A. Gardner, Ed., *Cyclostationary in Communications and Signals Processing*. New York: IEEE Press, 1994.

[51] W. A. Gardner, *Statistical Spectral Analysis: A Nonprobabilistic Theory*. Englewood Cliffs, NJ: Prentice-Hall, 1988.

[52] P. D. Sutton, K. E. Nolan, and L. E. Doyle, "Cyclostationary signatures in practical cognitive radio applications," *IEEE J. Sel. Areas Commun.*, vol. 26, pp. 13–24, Jan. 2008.

[53] C. M. Spooner, "Theory and application of higher-order cyclostationarity," Ph.D. dissertation, Dept. of Electrical and Computer Engineering, Univ. of California, Davis, CA, 1992.

[54] C. M. Spooner and W. A. Gardner, "The cumulant theory of cyclostationary time-series, Part II: Development and applications," *IEEE Trans. Signal Process.*, vol. 42, pp. 3409–3429, 1994.

[55] R. S. Roberts, W. A. Brown, and H. H. Loomism, Jr., "Computationally efficient algorithms for cyclic spectral analysis," *IEEE Signal Process. Mag.*, vol. 8, pp. 38–49, 1991.

[56] W. Bretl, W. R. Meintel, G. Sgrignoli, X. Wang, S. M. Weiss, and K. Salehian, "ATSC RF modulation, and transmission," *Proc. IEEE*, vol. 94, pp. 44–58, 2006.

[57] M. S. Bartlett, "Properties of sufficiency and statistical tests," *Phil. Trans. R. Soc. London A*, vol. 160, pp. 268–282, 1937.

[58] D. R. Brillinger, "The digital rainbow: Some history and applications of numerical spectrum analysis," *Can. J. Statist.*, vol. 21, pp. 1–19, 1993.

[59] M. G. Kendall and A. Stuart, *The Advanced Theory of Statistics*. New York: Hafner, 1963.

[60] D. J. Thomson, "Quadratic-inverse spectrum estimates: Applications to paleoclimatology," *Phil. Trans. R. Soc. London A*, vol. 332, pp. 539–597, 1990.

[61] M. Frigo and S. G. Johnson, "The design and implementation of FFTW3," *Proc. IEEE*, vol. 93, pp. 216–231, 2005.

[62] W. C. Jakes, *Microwave Mobile Communications*. New York: Wiley, 1974.

[63] T. Aulin, "A modified model for the fading signal at a mobile radio channel," *IEEE Trans. Veh. Technol.*, vol. VT-28, pp. 182–203, 1979.

[64] A. F. Molisch, L. J. Greenstein, and M. Shafi, "Propagation issues for cognitive radio," *Proc. IEEE*, vol. 97, May 2009.

[65] P. Setoodeh and S. Haykin, "Robust transmit power control for cognitive radio," *Proc. IEEE*, vol. 97, May 2009.

[66] J. F. Kaiser, "Nonrecursive digital filter design using the $I_0(\sinh)$ window function," in *Proc. IEEE Inter. Symp. Circuits Syst.*, 1974, pp. 20–23.

[67] S. O. Rice, *A Short Table of Values of Prolate Spheroidal Harmonics*," Bell Telephone Labs., MM 63-3241-13, 1963.

[68] B. Farhang-Boroujeny, "Filter bank spectrum sensing for cognitive radios," *IEEE Trans. Signal Process.*, vol. 56, pp. 1801–1811, May 2008.

[69] P. P. Vidyanathan, *Multirate Systems and Filter Banks*. Englewood Cliffs, NJ: Prentice-Hall, 1993.

ABOUT THE AUTHORS

Simon Haykin (Life Fellow, IEEE) received the B.Sc. (first-class honors), Ph.D., and D.Sc. degrees in electrical engineering from the University of Birmingham, U.K.

He is a pioneer in adaptive signal-processing with emphasis on applications in radar and communications, an area of research which has occupied much of his professional life. In the mid 1980s, he shifted the thrust of his research effort in the direction of Neural Computation, which was re-emerging at that time. All along, he had the vision of revisiting the fields of radar and communications from a brand new perspective. That vision became a reality in the early years of this century with the publication of two seminal journal papers: "Cognitive Radio: Brain-Empowered Wireless Communications," IEEE Journal on Selected Areas in Communications, February 2005; and "Cognitive Radar: A Way of the Future," IEEE Signal Processing Magazine, January 2006. Cognitive radio and cognitive radar are two important parts of a much wider and multidisciplinary subject: cognitive dynamic systems. The study of this emerging discipline has become the thrust of his research program at McMaster University, Ontario, where he is the Distinguished University Professor in the Department of Electrical and Computer Engineering.

Prof. Haykin is a Fellow of the Royal Society of Canada. He received the Henry Booker Medal from URSI, 2002, the Honorary Degree of Doctor of Technical Sciences from ETH Zentrum, Zurich, Switzerland, in 1999, and many other medals and prizes.

David J. Thomson (Fellow, IEEE) graduated from Acadia University, Wolfville, NS, Canada. He received the Ph.D. degree in electrical engineering from Polytechnic Institute of Brooklyn, Brooklyn, NY.

He retired as a Distinguished Member of Technical Staff from the Communications Analysis Research Department, Bell Labs, Murray Hill, NJ, in 2001, having previously worked on the WT4 Millimeter Waveguide System and Advanced Mobile Phone Service projects. He was an Associate Editor of *Radio Science.* In 2002, he became a Canada Research Chair in Statistics and Signal Processing in the Department of Mathematics and Statistics, Queen's University, Kingston, ON, Canada.

Dr. Thomson is a Professional Engineer. He is a member of the American Geophysical Union and the American Statistical Association; a Professional Statistician in the Statistical Society of Canada; and a Chartered Statistician in the Royal Statistical Society. He has been Chairman of Commission C of USNC-URSI and Associate Editor of the IEEE Transactions on Information Theory. He was a Green Scholar with Scripps Institution of Oceanography a Houghton Lecturer with the Massachusetts Institute of Technology, and has been awarded a Killam Fellowship by the Canada Council of Arts.

Jeffrey H. Reed (Fellow, IEEE) is the Willis G. Worcester Professor in the Bradley Department of Electrical and Computer Engineering, Virginia Polytechnic and State University, Blacksburg. From June 2000 to June 2002, he was Director of the Mobile and Portable Radio Research Group. He now is Director of the newly formed umbrella wireless organization Wireless @ Virginia Tech. His area of expertise is in software radios, cognitive radio, wireless networks, and communications signal processing. He is the author of *Software Radio: A Modern Approach to Radio Design* (Englewood Cliffs, NJ: Prentice-Hall, 2002) and *An Introduction to Ultra Wideband Communication Systems* (Englewood Cliffs, NJ: Prentice-Hall, 2005).